Article

Cell

Atoms to Phenotypes: Molecular Design Principles of Cellular Energy Metabolism

Graphical Abstract

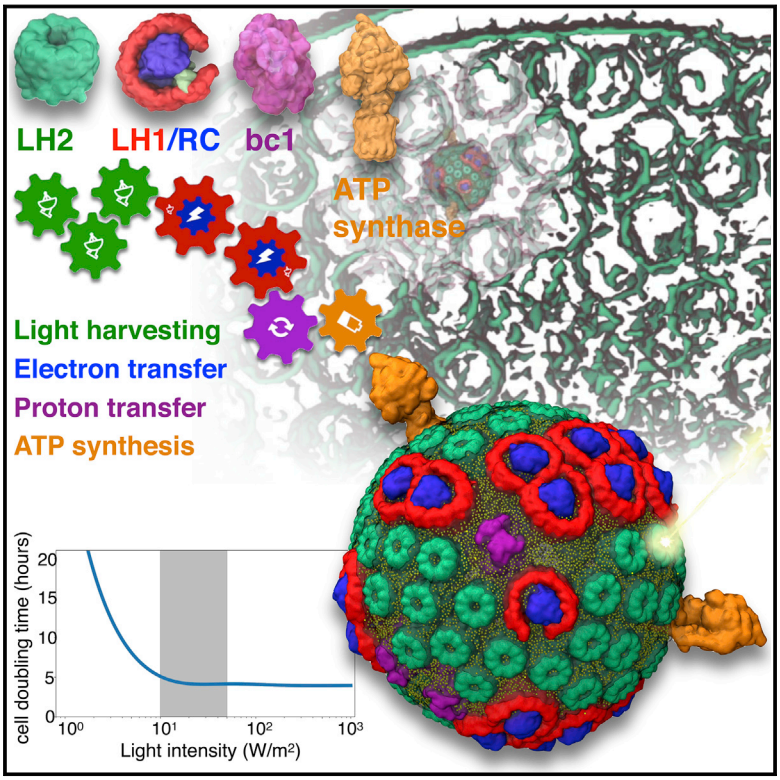

Authors

Abhishek Singharoy, Christopher Maffeo, Karelia H. Delgado-Magnero, ..., Emad Tajkhorshid, Aleksei Aksimentiev, Klaus Schulten

Correspondence

asinghar@asu.edu (A.S.), c.n.hunter@sheffield.ac.uk (C.N.H.), emad@life.illinois.edu (E.T.), aksiment@illinois.edu (A.A.)

In Brief

A full atomic resolution model of an entire organelle, the photosynthetic chromatophore vesicle of a purple bacterium, is constructed and reveals how the photosynthetic apparatus is optimized for ATP production in low-light habitats.

Highlights

- A cell organelle, the photosynthetic chromatophore, is modeled in atomistic detail
- Segregation of protein complexes tunes chromatophore structure and function
- The electrostatic environment of the organelle supports low light-adaptation
- Distinct modes of quinone diffusion underpin efficient electron transfer dynamics

Singharoy et al., 2019, Cell *179*, 1098–1111
November 14, 2019 Published by Elsevier Inc.
https://doi.org/10.1016/j.cell.2019.10.021

CellPress

Cell

Article

Atoms to Phenotypes: Molecular Design Principles of Cellular Energy Metabolism

Abhishek Singharoy,[1,13,14,*] Christopher Maffeo,[2,3,12] Karelia H. Delgado-Magnero,[4,12] David J.K. Swainsbury,[5,12] Melih Sener,[3,12] Ulrich Kleinekathöfer,[6,12] John W. Vant,[1,12] Jonathan Nguyen,[1] Andrew Hitchcock,[5] Barry Isralewitz,[3] Ivan Teo,[3] Danielle E. Chandler,[3] John E. Stone,[3] James C. Phillips,[3] Taras V. Pogorelov,[3,7,8,9] M. Ilaria Mallus,[6] Christophe Chipot,[2,3,10,13] Zaida Luthey-Schulten,[2,3,7,8] D. Peter Tieleman,[4,13] C. Neil Hunter,[5,13,*] Emad Tajkhorshid,[3,8,11,*] Aleksei Aksimentiev,[2,3,8,13,*] and Klaus Schulten[2,3]

[1]School of Molecular Sciences, Center for Applied Structural Discovery, Arizona State University at Tempe, Tempe, AZ 85282, USA
[2]Department of Physics, NSF Center for the Physics of Living Cells, University of Illinois at Urbana-Champaign, Urbana, IL 61801, USA
[3]Beckman Institute for Advanced Science and Technology, University of Illinois at Urbana-Champaign, Urbana, IL 61801, USA
[4]Centre for Molecular Simulation and Department of Biological Sciences, University of Calgary, Calgary, AB T2N 1N4, Canada
[5]Department of Molecular Biology and Biotechnology, University of Sheffield, Sheffield S10 2TN, UK
[6]Department of Physics and Earth Sciences, Jacobs University Bremen, 28759 Bremen, Germany
[7]Department of Chemistry, School of Chemical Sciences, University of Illinois at Urbana-Champaign, Urbana, IL 61801, USA
[8]Center for Biophysics and Quantitative Biology, University of Illinois at Urbana-Champaign, Urbana, IL 61801, USA
[9]National Center for Supercomputing Applications, University of Illinois at Urbana-Champaign, Urbana, IL 61801, USA
[10]Laboratoire International Associé CNRS-UIUC, UMR 7019, Université de Lorraine, 54506 Vandœuvre-lès-Nancy, France
[11]Departments of Biochemistry, Chemistry, Bioengineering, and Pharmacology, University of Illinois at Urbana-Champaign, Urbana, IL 61801, USA
[12]These authors contributed equally
[13]Senior author
[14]Lead Contact
*Correspondence: asinghar@asu.edu (A.S.), c.n.hunter@sheffield.ac.uk (C.N.H.), emad@life.illinois.edu (E.T.), aksiment@illinois.edu (A.A.)
https://doi.org/10.1016/j.cell.2019.10.021

SUMMARY

We report a 100-million atom-scale model of an entire cell organelle, a photosynthetic chromatophore vesicle from a purple bacterium, that reveals the cascade of energy conversion steps culminating in the generation of ATP from sunlight. Molecular dynamics simulations of this vesicle elucidate how the integral membrane complexes influence local curvature to tune photoexcitation of pigments. Brownian dynamics of small molecules within the chromatophore probe the mechanisms of directional charge transport under various pH and salinity conditions. Reproducing phenotypic properties from atomistic details, a kinetic model evinces that low-light adaptations of the bacterium emerge as a spontaneous outcome of optimizing the balance between the chromatophore's structural integrity and robust energy conversion. Parallels are drawn with the more universal mitochondrial bioenergetic machinery, from whence molecular-scale insights into the mechanism of cellular aging are inferred. Together, our integrative method and spectroscopic experiments pave the way to first-principles modeling of whole living cells.

INTRODUCTION

Living cells are brimming with the activity of hundreds of macromolecular complexes fulfilling their biological functions. Housed within subcellular compartments, so-called cell organelles, these complexes form an intricate circuitry of physicochemical reactions, giving rise to biological properties such as growth, adaptation to environmental change, and co-accommodation of competing functions. A physical model of the emergence of phenotypic properties from detailed atomistic interactions is expected to offer direct insights into the rules of life (Camargo, 2018). However, atomic-level investigations of cellular processes have so far been impeded by the sheer complexity of the network of interactions, the timescales of the cell cycle, and the lack of essential experimental information (Goh et al., 2016).

Bolstered by groundbreaking developments in high-resolution imaging (Rust et al., 2006) and cryo-electron microscopy (Cheng, 2015), the atomic structures of many protein complexes are now experimentally accessible. However, structures alone provide limited information about the function of these complexes, in particular how they interact with each other in large-scale networks. Bioinformatics and systems biology approaches integrating libraries of existing experimental data have attempted to predict phenotypes from genotypes (Karr et al., 2012). The resulting models, however, can be plagued by false positives, often originating from experimental errors or mathematical heuristics (Korte and Farlow, 2013). Cell-scale models conceived from first principles can resolve the physical and chemical events that underlie the emergent phenotypes and ultimately render a comprehensive picture of the cellular machinery in action.

Here, we employ an array of physics-based approaches to decipher the functional circuitry of a bacterial energy-harvesting organelle, the chromatophore (Allen, 2017; Blankenship, 2014).

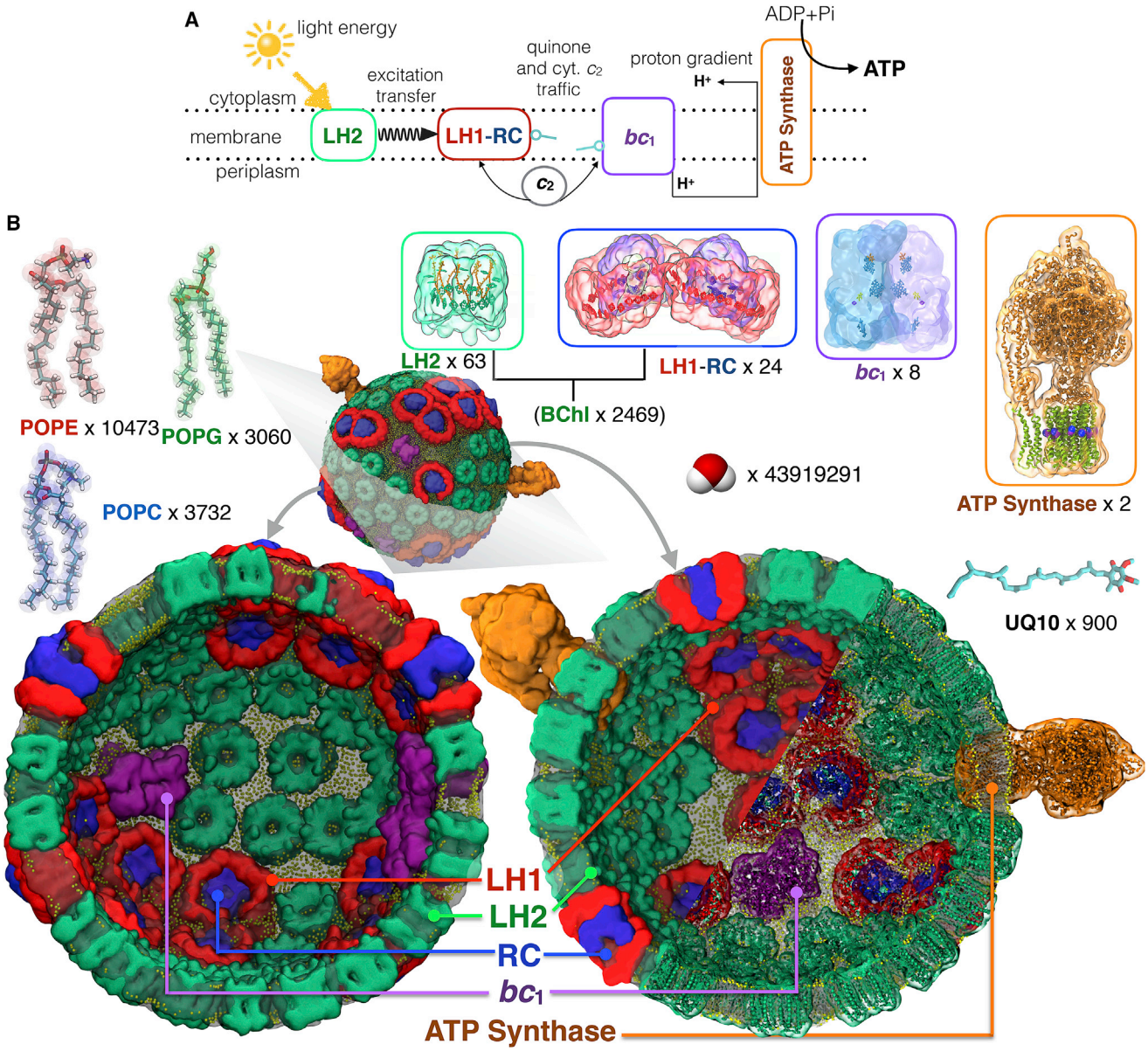

Figure 1. Physical Model of a Chromatophore

(A) Photosynthetic energy conversion in a purple bacterial chromatophore. Light energy absorbed by light-harvesting LH2 and LH1 complexes is channeled to the reaction center (RC), where a charge separation is stabilized as a reduced quinone, and the electron hole is filled by reduced cyt c_2. Subsequent turnovers of the bc_1 complex generate a proton-motive force that drives ATP synthesis.

(B) All-atom model of the chromatophore from the purple bacterium *Rba. sphaeroides*. Illustrated using two halves of a transverse section, the final configuration of the all-atom model was obtained after 0.5 μs of explicit solvent all-atom equilibrium MD simulation. The model features 82 bioenergetic complexes (63 light-harvesting LH2 complexes [green], 11 dimeric and 2 monomeric RC-LH1 complexes [LH1, red; RC, blue], 4 bc_1 dimers [magenta], and 2 ATP synthases [orange]), together with 4,011 light-absorbing antenna molecules (2,469 BChls and 1,542 carotenoids) embedded in a membrane of approximately 17,200 lipid molecules (lipid phosphate is indicated in yellow). The vesicle is embedded in a rectangular volume of explicit water (shown in SI) and 4,624 sodium ions to ensure neutrality. The simulation system consists of 136,833,034 atoms and measures 112 × 112 × 112 nm.

With hundreds of proteins embedded in a vesicular membrane (Figure 1), the chromatophore from *Rhodobacter sphaeroides* (*Rba. sphaeroides*) absorbs sunlight to produce ATP. We explore, in atomistic detail, the pathways of energy metabolism within chromatophore vesicles to determine how light-specific phenotypes of purple bacteria emerge from the collective action of proteins. Our simulations identify the mechanisms that bioenergetic protein networks commonly exploit to minimize energy dissipation, recover from environmental stresses, and avoid apoptosis. More broadly, we elucidate how the physicochemical

Table 1. Table Summarizing All Simulations Employed in the Current Study

Simulation Type	Simulation System	System Size	Number of Runs	Simulation Length	Cumulative Time
MD	chromatophore vesicle	136 M	1	0.5 μs	0.5 μs
ZNDO/S-CIS	63 LH2 rings (vesicle)	63 × 1M	200 snapshots	50 ps	10 ns
ZNDO/S-CIS	1 LH2 rings (flat)	0.2 M	10,000 snapshots	1 ps	10 ns
MARTINI	1 bc_1 complex	0.06 M	1	40 μs	40 μs
BD	500 copies of cyt. c_2	N/A	6	10 μs	30 ms
	5,000 quinone molecules	N/A	1	2.8 ms	2.8 ms
Bias exchange umbrella sampling	1 × bc_1ox-$c_2$red	0.5 M	34 windows	100 ns	3.4 μs
	1 × bc_1red-$c_2$ox	0.5 M	34 windows	100 ns	3.4 μs
	1 × RCox-$c_2$red	0.5 M	34 windows	100 ns	3.4 μs
	1 × RCred-$c_2$ox	0.5 M	34 windows	100 ns	3.4 μs
	1 × bc_1ox-$c_2$red (20 mM)	0.5 M	34 windows	100 ns	3.4 μs

reactions within a membrane-based cellular organelle are wired to preserve the delicate balance between structural integrity, robust energy conversion, and cellular growth.

RESULTS

A Physical Model of the Chromatophore

The bacterial chromatophore converts light into ATP in a multi-step process (Figure 1A; Video S1). First, light is absorbed by the LH2 and LH1 light-harvesting complexes, and then the energy migrates to the reaction center (RC), where charge separation by electron transfer occurs. The outcome is a reduced quinone (quinol) that leaves the RC and diffuses to the cytochrome bc_1 (bc_1) complex, where a proton-motive force is generated for the synthesis of ATP. Abstraction of an electron from bc_1 by cytochrome c_2 (cyt c_2), and docking of this reduced cyt c_2 fills the electron hole in the RC and resets the system for another charge separation. We have developed several first-principle models that reflect the complexity of these coupled energy-conversion processes and link the microscopic configuration of the proteins within the chromatophore membrane to the rate of ATP synthesis and, hence, to the phenotype of the bacterium.

An atomistic model of the *Rba. sphaeroides* chromatophore is composed of proteins, lipids, cofactors, and charge carriers immersed in water and ions. Illustrated in Figure 1B, this model builds on earlier versions (Sener et al., 2007, 2010) based on atomic-force microscopy (AFM) (Bahatyrova et al., 2004; Olsen et al., 2008; Adams and Hunter, 2012; Cartron et al., 2014), electron microscopy (Qian et al., 2008; Cartron et al., 2014), crystallography (Qian et al., 2013), mass spectrometry (Jackson et al., 2012; Cartron et al., 2014; Woronowicz and Niederman, 2010), and optical spectroscopy (Dahlberg et al., 2017). The 136-million-atom fully hydrated chromatophore vesicle had an average inner diameter of 52 nm (Adams and Hunter, 2012) and contained 82 bioenergetic complexes together with 4,011 light-absorbing antenna molecules embedded in a membrane of 17,200 lipid molecules containing 22% POPC, 22% POPG, and 56% POPE in the outer, cytoplasmic side of the vesicle and 24% POPC, 10% POPG, and 66% POPE in the inner, periplasmic side (Cartron et al., 2014). In addition, 600 quinone (ubiquinone-10) charge carriers were uniformly placed within the membrane, and another 300 were placed in the vicinity of the bc_1 and RC-LH1 complexes (Sener et al., 2016).

The initial all-atom model of the chromatophore was simulated by all-atom molecular dynamics (MD) (Karplus, 2014) for more than half a microsecond (Table 1 and Figures S1). The simulation revealed changes in local curvature and composition of the lipid membrane surrounding the proteins, and characterized dynamics of quinone molecules in the membrane. The resulting molecular configurations were used to determine the effect of membrane disorder on light absorption as well as to elucidate the principles of directional charge transport within the vesicle. Rates of individual processes were integrated into a kinetic model of ATP synthesis. This integrated model captures the emergence of light-adaptation phenotypes in purple bacteria starting from all-atom details. Further details regarding the pros and cons of our model are provided in Method Details.

Segregation of Proteins Enables Heterogeneous Membrane Curvature

Analysis of the MD trajectory shows protein-driven heterogeneity in membrane curvature and its impact on energy transfer processes. The shape of a chromatophore departs from that of an ideal sphere, displaying distinct protein-sculpted features on the surface (Figure 2). Specifically, the local curvature in the vicinity of the LH1 dimers or of hexagonally packed LH2 complexes is closed (convex), with a radius of 200–250 Å, whereas curvature in the vicinity of the bc_1 complex is flatter, with a radius of 400–500 Å (Figures 2A and 2B). A 40-μs coarse-grained MD simulation (Marrink et al., 2007) confirmed the curvature modulations observed in the 0.5-μs all-atom MD simulation (Figure 2C), reinforcing our conclusion that the shape of bc_1 dimers is compatible with that of a planar membrane.

Differences in membrane curvature near the LH1, LH2, and bc_1 complexes (Figures 2D and 2E) are a manifestation of the uneven hydrogen bonds they form with the lipid head groups on the cytoplasmic and periplasmic sides of the membrane bilayer (Figures S2A–S2C). The RC-LH1 dimers and hexagonally packed LH2 complexes form 3- to 4-fold more hydrogen bonds on the cytoplasmic side of the chromatophore than on the periplasmic side, introducing curvature in the membrane (Olsen

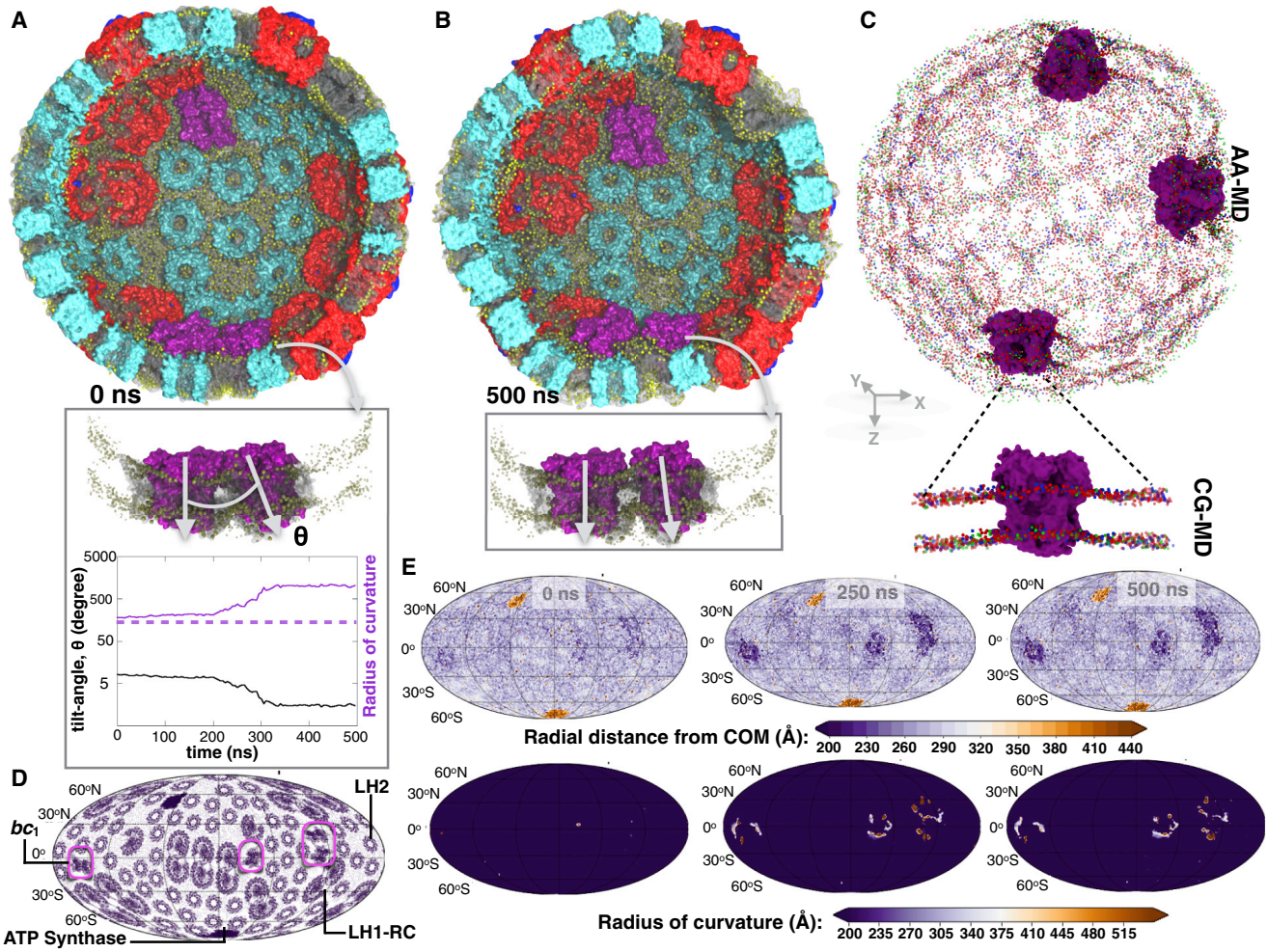

Figure 2. MD Simulation Reveals Protein-Specific Heterogeneity of Membrane Curvature

(A and B) Snapshots of the chromatophore vesicle at the beginning (A) and after 500 ns (B) of the MD simulation. The membrane is nearly flat in the vicinity of the bc_1 complexes (magenta) but convex near other proteins (see also Figure S2D). Insets: enlarged views of the two proximal bc_1 complexes that induce the largest change in local membrane curvature. The tilt angle (θ) between the two proximal bc_1 complexes decreases during the simulation, reflecting a gradual increase in the local radius of curvature (the tilt angle-radius of curvature relationship is discussed in Method Details: Equation 3). A dotted line indicates the radius of the membrane vesicle at the beginning of the MD simulation (Figure S1C).

(C) Flat-to-convex curvature in the vicinity of the bc_1 complexes observed in the all-atom (AA) and coarse-grained (CG) MD simulations; phosphate head groups of POPE, POPG, and POPC are shown as red, green, and blue beads, respectively.

(D) 2D Mollweide projection map of the chromatophore vesicle with the four types of membrane protein complex annotated.

(E) Top: Mollweide projection maps of the chromatophore membrane, illustrating the radial distances of its atoms to the vesicle's center of mass at 0, 250, and 500 ns of the AA MD simulation. The distance is highest for the protruding ATP synthase motors, smallest for the bc_1-rich areas, and almost uniform across the rest of the chromatophore membrane. Bottom: local radius of curvature at every point on the chromatophore, derived using a 2D curve fitting protocol (Method Details: Equations 1 and 2) at 0, 250, and 500 ns of AA MD. The radius of curvature is uniform across the chromatophore, except for the bc_1-rich patches, where the membrane is considerably flatter, and the radius exceeds 500 Å.

et al., 2008). In contrast, hydrogen bond mismatch is minimal for bc_1 complexes, eliciting a flatter topography in their vicinity. This protein-induced reshaping of the chromatophore membrane (Figure 2E) supports the hypothesis of segregation of bc_1 from LH1 and LH2 derived from AFM experiments (Cartron et al., 2014; Kumar et al., 2017). We find that the proteins with strong curvature dependence, such as the dimeric RC-LH1-PufX and LH2 of *Rba. sphaeroides* (Frese et al., 2008; Olsen et al., 2008), are packed together into a spherical arrangement (Chandler et al., 2008), whereas those agnostic to curvature (bc_1) are sequestered within isolated domains that become locally flat. Thus, deviation of the membrane from an ideal sphere (Noble et al., 2018) allows co-localization of groups of proteins into neighborhoods with distinct curvature-dependent functions. The hydrogen bonding pattern in bc_1 induces such local curvature differences, supporting organelle budding.

To elucidate the effect of membrane disorder and local curvature on light absorption by LH2, large-scale QM/MM

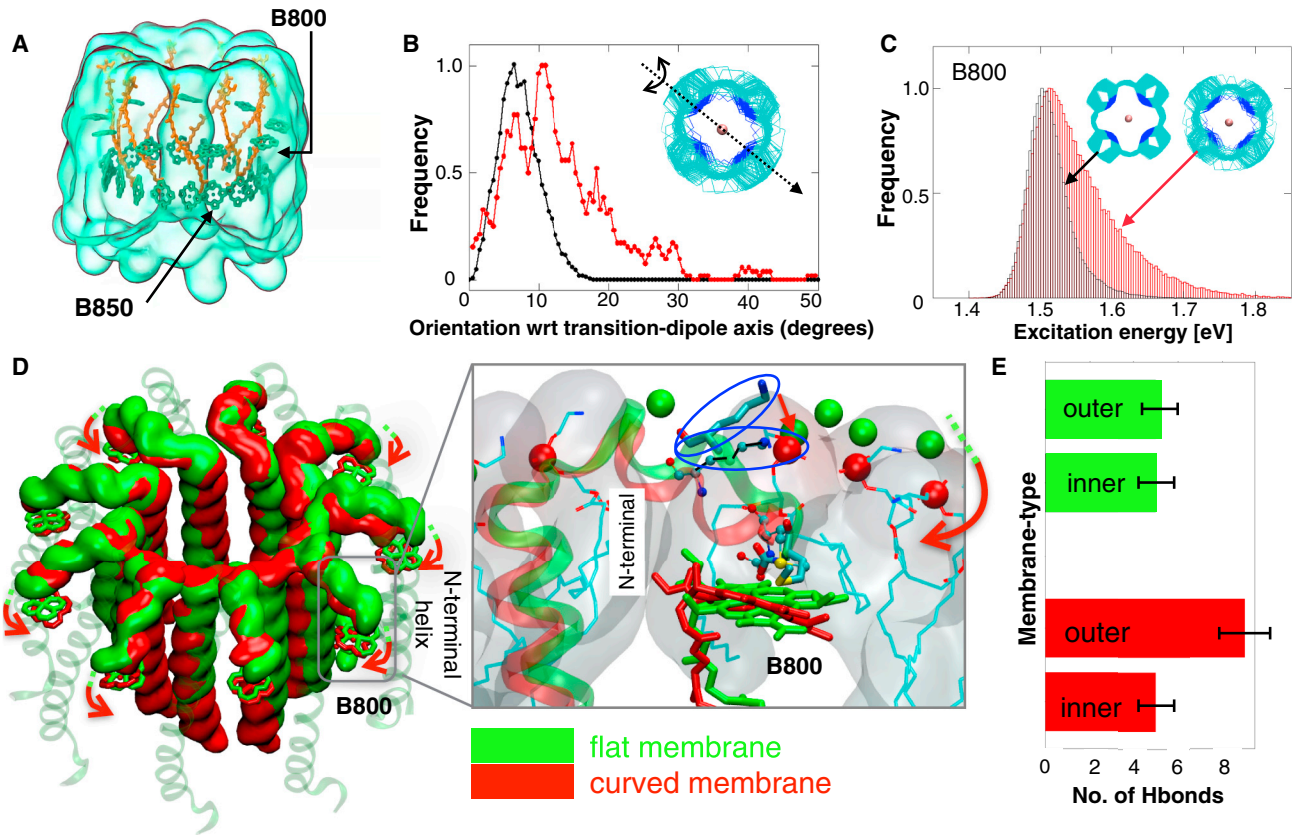

Figure 3. Thermal Disorder in the Chromatophore Membrane Modifies Inter-pigment Excitation Transfer

(A) The structure of LH2 pigments, indicating the arrangement of B800 and B850 BChl molecules. Each LH2 complex is composed of a ring of nine B800 molecules oriented perpendicularly to nine pairs of B850 molecules. Nine carotenoid molecules are also shown in orange.

(B) Orientation of the B800 pigments relative to their crystallographic geometry (PDB: 1NKZ) about the transition-dipole, NB-ND axis (inset) (Ogren et al., 2018) for LH2 in the flat membrane (black) versus the chromatophore (red). A statistical shift in the B800 orientation angles of 11° relative to the crystallographic geometry is observed.

(C) Distributions of excitation energies in BChl B800 for the simulation of a single ring in a flat membrane (black) and for all rings in the chromatophore (red), indicating line broadening. (inset) A scatter diagram of the B800 molecules depicts a broader range of orientations in the chromatophore than in a flat membrane (also shown in Figure S2F).

(D) Large-scale conformational transition observed when LH2 is simulated in a flat (green) versus a curved (red) membrane because of reorientation of the C-terminal helices. Inset: close-up view of the N-terminal helix, showing arginine residues (represented in CPK and outlined in blue) engaged in formation of additional hydrogen bonds with the phosphate head groups (indicated in red) to induce curvature. Accommodation of these interactions results in reorganization of the N-termini, which directly coordinate with the Mg^{2+} ion of B800, reorienting the porphyrin ring. Minimal reorganization is observed on a flat membrane (indicated in green).

(E) Distribution of hydrogen bonds between LH2 and phosphate head groups, showing a mismatch in the curved membrane, which induces the conformational changes depicted in (D).

computations were performed. The ZINDO/S-CIS level of theory was used with atomic models extracted from the all-atom MD simulations. These simulations showed that the light-absorbing rings of LH2 B800 bacteriochlorophyll (BChl) deviate from their crystallographic orientations by tilt angles ranging from 0° to 30° about the transition-dipole axis (Figures 3A and 3B). Such a reorientation of the B800 rings within the chromatophore has been implicated in the enhancement of the energy transfer rate from the B800 to B850 BChls (Ogren et al., 2018). The QM/MM computations indicate a selective broadening of the B800 absorption band relative to B850 (Figures 3C and S2) as well as a wider distribution of the ring-averaged excitation energies. The 10-meV width of the excitation energy distribution (Figure S3) is similar to values of 7.4 and 9.4 meV previously extracted from pump-probe experiments (Stross et al., 2016). Our simulation identifies two factors that influence reorientation and spectral broadening of B800. First, curvature-specific rearrangement of the N-terminal domains of LH2 at the protein-lipid interface reorients the B800 pigments to unique conformations observed only in the chromatophore (Figure 3D). Second, the lipid tails in the local environment of B800 are 1.25- to 2-fold more disordered than those in a flat membrane (Figures S3B–S3F; Yesylevskyy et al., 2017), which allows fluctuation in the orientation of B800 pigments and consequent broadening of inter-pigment couplings. In contrast, the B850 rings are minimally exposed to the lipid tails, and little line

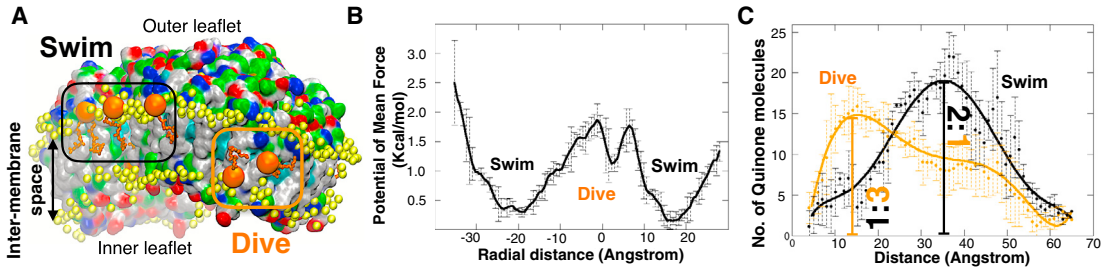

Figure 4. Dynamics of Quinone Molecules Reveal a Two-State Model of Membrane-Mediated Charge Transport

(A) Snapshot in the vicinity of an LH1 protein, illustrating the two modes of charge carrier quinone arrangement within the chromatophore membrane. "Swimming" involves diffusion with the quinone head group (orange beads) in the same plane as those of the lipids (yellow beads), whereas "diving" features passage of the head group through the intra-membrane space lined by lipid tails.

(B) PMF of a quinone molecule as a function of its location in the membrane, defined along a line passing through the center of the chromatophore and the local midplane of the membrane (0 Å). The two most stable regions (at ±20 Å) correspond to swimming quinones on the inner and outer leaflets of the chromatophore membrane, whereas the center is preferred by the quinones in the diving state.

(C) Number of quinones as a function of distance from the surface of the RC-LH1 protein. The swimming quinones are more abundant at larger distances from the protein, whereas diving quinones are found predominantly near the protein surface. Smooth solid lines represent sixth-order polynomial fits to the average quinone count per 1-Å distance bin (black or orange circles).

broadening is observed. Altogether, the selective reorientation of pigments and broadening of their absorption spectrum accentuate the role of the lipid environment in modulating light absorption by the chromatophore.

The Quinone Pool Employs Two Distinct Modes of Diffusion for Mediating Membrane-wide Charge Transfer

Charge-carrier quinone molecules transfer energy between the protein complexes of the chromatophore by shuttling electrons from RC-LH1 to bc_1 (Figure 1A). The energy conversion efficiency of the entire network therefore is expected to depend on the diffusion and binding dynamics of the quinone (Sener et al., 2016). These charge-transfer processes were simulated with atomistic detail to probe the rate-determining step of energy conversion from sunlight intake to ATP output.

Analysis of the diffusion of 900 quinone molecules in the chromatophore shows two distinct types of motion the quinones perform within a membrane: swimming and diving Figure 4A. The probability of finding a quinone at different depths of the membrane was monitored using potential of mean force (PMF) calculations (Method Details: Umbrella Sampling Simulations). These calculations indicate that the dione head groups of swimming quinones are located within the plane of the lipid head groups, whereas those of diving quinones are found near the membrane midplane (Figure 4B). The calculated diffusion coefficient of the swimming quinones (7.7×10^{-8} cm^2 s^{-1}) is comparable to that of bulk lipids. In contrast, the diving quinones diffuse at least three times faster (2.1×10^{-7} cm^2 s^{-1}) (Figure S4A). Although both values are well within the 10^{-6}-10^{-8} cm^2 s^{-1} range of measured quinone diffusivities (Di Bernardo et al., 1998), our computations clearly distinguish between the two distinct diffusion mechanisms that collectively contribute to this apparently wide range of experimental values. Employing the PMF of Figure 4B and integrating the two modes of quinone dynamics into a spatially dependent diffusion map (Method Details: BD Simulations), Brownian dynamics (BD) simulations (Ermak and Mccammon, 1978) were performed to measure the rate of diffusive quinone transport within the chromatophore. These computations yielded a mean first passage time of 101 μs for the quinone movement between the RC-LH1 and bc_1 complexes (Figure S4).

Remarkably, the ratio of swimming to diving quinones depends on the local protein content of the membrane. The swimming-to-diving quinone ratio is approximately 2:1 in lipid-rich environments away from the protein complexes (Figure 4C). This ratio switches to 1:3 in the vicinity of proteins, with a majority of quinones diving to the membrane mid-plane. Employing the Szabo-Schulten-Schulten equation (Szabo et al., 1980), we found an interconversion time from swimming to diving of ~220 ns (Method Details: Mean First Passage Time Computation). The two modes of quinone dynamics suggest the following model of membrane-mediated charge transport in the chromatophore. (1) Quinones primarily swim in bulk membranes with head groups parallel to the lipid head groups. In the chromatophore, this diffusive motion spans the sub-millisecond timescale. (2) Close to the protein complexes, quinones sense the electric field created by the binding pockets (Figure S4B) and move toward the middle of the membrane within a few hundred nanoseconds. Because most of the quinone binding pockets are buried within the membrane, diving provides an energetically feasible pathway for the quinone to access these pockets with minimal reorganization of the proteins. A swimming quinone would require more substantial protein reorganization to elicit binding, slowing electron transport. (3) Finally, the diving quinone diffuses into the binding pocket.

A typical quinone turnover process includes its unbinding from the bc_1 complex, migration to the RC-LH1, encounter with the external face of this complex, finding the single pore adjacent to PufX (Qian et al., 2013), moving through the "breathing" pore past up to ten already trapped quinones in the space between the RC and the inner face of LH1, then finally docking into the RC quinone binding site. A simple model excluding the effect of cooperative inter-quinone interactions indicates that the

binding-unbinding time for quinone to the RC-LH1 is about 8 ms (Aird et al., 2007); accounting for the cooperative interactions offsets the binding kinetics by approximately 1 ms (Comayras et al., 2005b). In contrast, the binding rate of the quinol to bc_1 or the RC is an order of magnitude faster than that of quinone to the RC (Bazil et al., 2013). The diving motif applies to both quinone and quinol because both share similar binding pockets. Quinol is more polar than quinone, correlating with faster binding to the pocket (Pingale et al., 2018). With the RC-to-bc_1 diffusion time of 101 μs determined here (Figure S4C), we infer that the rate-determining step is not the nm-scale diffusion of the quinone in the bilayer, even while traversing the densely packed LH2 environment (Cartron et al., 2014), but, rather, its angstrom-scale binding from RC-LH1 and the associated conformational changes in the quinone-binding pocket. This agrees with dynamic light scattering and NMR studies of quinone-binding kinetics (Milano et al., 2003), which put the time of reversible quinone binding to RC-LH1 anywhere between 2–25 ms, much slower than the microsecond timescale of the through-membrane quinone diffusion (Milano et al., 2003). Our result is also consistent with findings from fluorescence spectroscopy and redox titrations. With one-third of the RCs inhibited, the extent of the quinone pool was decreased by about 10%, implying RC-quinone interaction and not quinone diffusion as a rate-determining process (Comayras et al., 2005a). Furthermore, at low temperatures (−20°C), where mobility is reduced, multiple turnovers of the quinones still occur, determined by the reaction rate at the RC (200 ms, an order of magnitude slower than observed at room temperature) (Comayras et al., 2005b). All these results collectively implicate the quinone turnover at RC-LH1 to determine the rate of energy turnover within the chromatophore.

Because quinones are ubiquitous in multiple bioenergetic networks, the turnover dynamics simulated here are expected to have important functional consequences. For instance, within the inner mitochondrial membrane, quinol molecules are actively oxidized near the P side of the membrane, whereas quinones are reduced on the N side, complemented by the release and uptake of protons, respectively (Wikström et al., 2015). A quinone population formed upon oxidation on the P side, such as by the activity of mitochondrial bc_1 (complex III), would flip to the N side to reach complex I for reduction (Kaurola et al., 2016). Consistent with our results, such a scenario would require that quinones flip rapidly in the inner mitochondrial membrane, which is critical for optimal turnover of the entire electron transport chain. Fourier transfer infra-red (FTIR), electron paramagnetic resonance (EPR) spectroscopy, and high-resolution cryoelectron microscopy (cryo-EM) are proposed in Method Details as ways of observing the two modes of quinone movements in membranes. FTIR experiments are sensitive to shifts in the spectroscopic signal of molecules when they are immersed in media of different viscosities; e.g., water versus lipids (Hellwig, 2015). EPR, on the other hand, is performed with spin-labeled quinones in artificial spin-labeled membranes, where a diving motion is expected to quench spin-spin coupling that is observed in the swimming mode (Pohl et al., 2010; Sahu et al., 2013). Finally, high-resolution cryo-EM has identified a quinone in a membrane location compatible with diving mode (Qian et al., 2018).

Robust Electrostatic Environment of Chromatophore Interior Sustains Unidirectional Cyt c_2 Dynamics

The interior of the chromatophore, the lumen, sequesters cyt c_2 molecules, which shuttle electrons from bc_1 to RC-LH1. This step closes the electron chain that began with the transport of electrons and protons from RC-LH1 to bc_1 via the quinones (Figure 1A). Recognition, binding, and unbinding of cyt c_2 to the integral-membrane complexes are driven by the charge state of the chromatophore vesicle (Hunte et al., 2002; Berry et al., 2000; Singharoy et al., 2016). We characterized this charge state by using continuum electrostatics approximations (Baker et al., 2001) between pH values of 6 and 7 and periplasmic salt concentrations of 0.15–0.95 M, where the effective charge of the chromatophore model is found to be conserved (Figure 5A). This conserved charge state allows cyt c_2 turnover to be functionally robust across multiple environmental conditions.

The influence of the charge of the chromatophore lumen on cyt c_2 dynamics was further investigated using BD simulations. The aim was to determine how the mechanism of cyt c_2 binding is attuned to maintaining a preferred direction of electron transport within reduced and oxidized chromatophore states. In the reduced chromatophore, the heme groups in the bc_1 complexes were modeled as reduced, the RC was kept neutral, and cyt c_2 was oxidized. In the oxidized chromatophore, the electronic charge was removed from bc_1 and placed onto the cyt c_2 heme, and the RC was oxidized. The averaged electrostatic maps derived at pH 7 and 0.15–0.25 M salinity were used as the driving potentials in BD.

The association times of cyt c_2 to the bc_1 and the RC-LH1 complexes were 13 and 70 ns in BD simulations at 0.15 M salinity, respectively (Figure S5). The cyt c_2 binding of these complexes is robust to changes in architecture of the chromatophore model (Figure S6). Additionally, the times for reversible cyt c_2 binding (combining its association and dissociation times) of bc_1 and RC were found to be 1 and 0.2 ms, respectively, using umbrella sampling simulations (Figure S7). Thus, the cyt c_2 shuttling time is found to be much faster than that for cyt c_2 association and binding. Under reducing conditions, the association between the reduced bc_1 complex and the oxidized cyt c_2 is favored (Figures 5B, S5, and S7). In contrast, the affinity of reduced cyt c_2 for the RC-LH1 complex increases within the oxidized chromatophore. As a consequence, the cyt c_2 in a reduced chromatophore can recognize the bc_1 surface, dock onto it, and accept an electron. Release of the electrons from bc_1 to cyt c_2 resets the local chromatophore environment to the oxidized state, within which the reduced cyt c_2 now targets the acceptor RC-LH1 complexes, facilitating directional bc_1-to-RC-LH1 electron transport. The reverse electron-transport pathway (unbinding of the reduced cyt c_2 from RC and rebinding to bc_1) is rendered unfavorable by redox-induced changes in the protein-protein interfacial interactions (Figure S7C); the cyt c_2-RC interactions in a reduced chromatophore are weaker than those under oxidizing conditions (Vasilev et al., 2014), and, conversely, the cyt c_2-bc_1 interactions within a reduced chromatophore are stronger than those under oxidizing conditions. As a result, the electron will remain with bc_1 under reducing conditions, and movement to the RC is avoided. Electron bifurcation within the bc_1 complex creates a proton gradient,

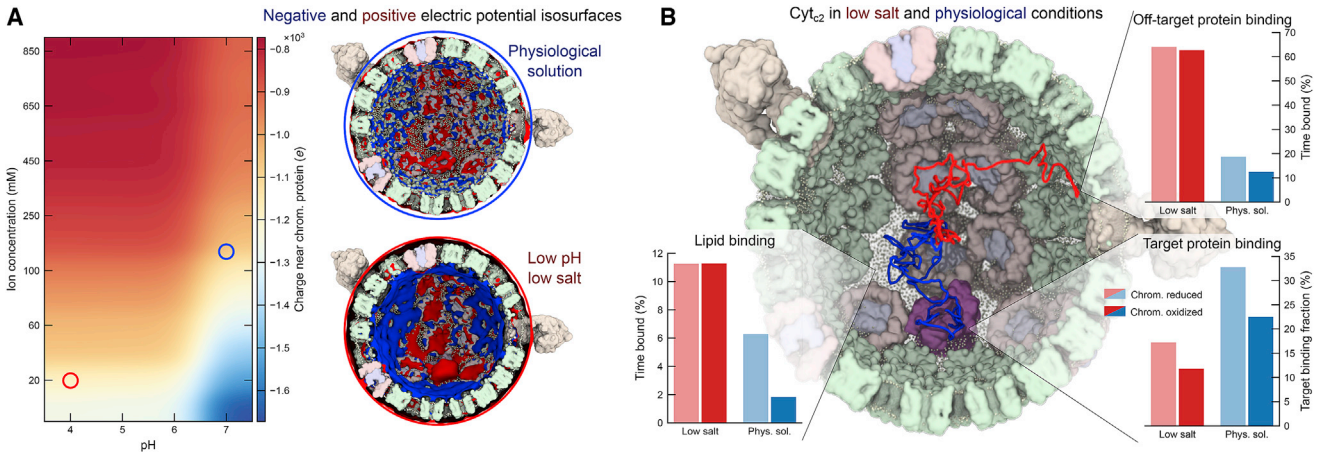

Figure 5. Phase Diagram of Chromatophore Activity Showcases Design Principles for Efficient Organelle-Scale Single-Electron Transport

(A) Dependence of chromatophore electrostatics on pH and ion concentration. The heatmap shows the average charge of the chromatophore, including solvent and fixed contributions, within 1 nm of the membrane surface, as calculated using APBS. The images depict 0.1 (blue) and −0.1 (red) kT electrostatic isosurfaces for low-salinity (pH 4, 0.02 M; bottom, red circle) and physiological conditions (pH 7, 0.15 M; top, blue circle).

(B) Effect of solution conditions on cyt c_2 targeting efficiency from BD simulations. The central image depicts two independent representative traces of cyt c_2 moving through reduced chromatophores under low-salinity (red) and physiological conditions (blue). For each condition, 500 simulations of a single cyt c_2 were performed, each simulation lasting 10 μs. The cyt c_2 molecules were all initially in the center of the chromatophore. The trajectories provided the time the cyt c_2 spent within 1 nm of off-target proteins, lipids, and target proteins, as depicted in the bar charts on the left. Although surface binding is enhanced overall, the targeting efficiency, or the ratio of the likelihood of being in contact with a target protein compared with an off-target protein, is considerably lowered under low-salinity conditions, as shown in the bar chart on the right.

bolstering the thermodynamic feasibility of energy conversion in the forward direction of ATP synthesis. Under oxidizing conditions, the electron will be transferred to cyt c_2 and move toward any of the available RC-LH1 complexes, closing the electron transport chain (Authenrieth et al., 2004).

Environmental Stress Switches the Rate-Determining Step for ATP Generation

The electrostatic landscape (Figure 5A) depicts a number of distinct biological scenarios. The physiological conditions for chromatophore function are at pH 7 and 0.15 M salinity (Blankenship, 2014). A low pH corresponds to an over-acidification of the membrane, a condition that can arise due to high illumination when proton translocation by bc_1 and RC-LH1 exceeds its consumption by ATP synthase (Geyer et al., 2010). Low salinity of the medium, on the other hand, is generally ascribed to aging and apoptosis artifacts in bioenergetic networks (Yu and Choi, 2000). Because the dynamics of quinone are independent of the charge state of the chromatophore (Madeo and Gunner, 2005), BD simulations of cyt c_2 were repeated for 10 ms at pH 4 and 0.02 M salinity to investigate the mechanisms of electron transport under stress.

Higher levels of non-specific cyt c_2 binding were observed under low-pH and low-salinity conditions compared with physiological conditions—an expected observation because the effective charge of the chromatophore is highest in the former case (Figure 5A). Surprisingly, a significant number of trajectories indicate that cyt c_2 binds to the anionic POPG lipids of the chromatophore membrane instead of the target proteins. Thus, cyt c_2 binding to the bc_1 and the RC-LH1 complex is only marginally enhanced under low-pH and low-salt conditions, resulting in an overall decrease in the recognition/targeting efficiency of cyt c_2 (the ratio of the likelihood of cyt c_2 being in contact with a bc_1 or RC compared with it being in contact with the rest of the chromatophore; Figure 5B). Under physiological conditions, however, charges from the lipids are effectively screened, and the targeting efficiency of cyt c_2 vastly improves, allowing efficient $bc_1 \rightarrow$RC-LH1 charge transport to sustain a healthy rate of ATP synthesis downstream. In line with EPR measurements (Sarewicz et. al., 2008), the cyt c_2-bc_1 and cyt c_2-RC association times increase, respectively, to 27 and 25 μs at 0.02 M salinity relative to 13 and 70 ns at 0.15 M (Figure S5B). Similarly, the cyt c_2 turnover, or reversible binding time, increases from 1 ms to 71 ms (Figure S7). Because the binding time of quinone is 8 ms (Aird et al., 2007), slower than that of cyt c_2 under physiological conditions (Gerencsér et al., 1999), quinone turnover at RC-LH1 is clearly the rate-limiting charge-transfer step in native chromatophores. However, at 0.02 M salinity, the barrier against cyt c_2 unbinding is significantly higher (Figure S7A). Thus, under salt stress, the rate-determining event switches from quinone binding to cyt c_2 turnover. This agrees with steady-state flash photolysis measurements of chromatophores at low salt concentrations, where cyt c_2 binding kinetics have been implicated as a rate-determining bottleneck for ATP generation (Tian et al., 2000; Hall et al., 1987; Engstrom et al., 2002). The internal redox activity of the integral membrane proteins changes minimally with salt conditions (Xia et al., 2013; Kimura et al., 2009).

The slower timescale for cyt c_2 turnover at low salt strengths enhances the statistical probability of electron leakage in this bioenergetic network. For example, potential entrapment of the cyt *c*-based electron carriers by anionic lipids now increases (Figure 5), promoting the feasibility of free radicals in the cell

membrane (Yu and Choi, 2000). A fraction of the electron flux is diverted from the photosynthetic energy conversion cycle into formation of reactive free-radical species. Such dissipation of the electron transport manifests itself in loss of the proton gradient across the bc_1 complex, resulting in a reduced yield of ATP synthesis. This finding bears a remarkable similarity to mitochondrial bioenergetics. Low salinity enhances anionic lipid binding of cyt *c* and prevents their release from the inner mitochondrial membrane, triggering apoptosis or aging of the ATP-starved cells (Yu and Choi, 2000; Green, 2005). Analogous to the dynamics of cyt c_2 in the chromatophore, cyt *c* under native salt conditions is released by the mitochondrial membrane, and normal operation of the network resumes.

Architecture of the Chromatophore Supports Low-Light Adaptation Phenotypes

The emergence of phenotypic properties from all-atom dynamics was captured by employing a kinetic model of energy turnover. The ATP production rate, k_{ATP}, of a chromatophore is found to be

$$k_{ATP}(I) = \frac{1}{2} Iq \left(1 + \frac{1}{2} Iq\tau(I) \frac{1}{n_{RC}}\right)^{-1},$$

where I is the intensity of incident sunlight, q is the quantum yield, n_{RC} is the number of RC-LH1 complexes, and τ is the time of electron transport between RC-LH1 and bc_1 (Sener et al., 2016). Under physiological conditions, τ represents the quinone cycling time at the RC-LH1. However, at pH 4 and 0.02 M salinity (i.e., under conditions of low-salt stress), the rate-determining step for electron transport switches, and τ is now determined by the kinetics of cyt c_2 turnover at bc_1. Our all-atom model of the chromatophore together with MD and BD simulations offers direct measurements of these turnover times, reported already in the previous sections. In moving toward a model that predicts cell-scale properties starting from a full atomistic picture, we use these kinetic equations to calculate ATP turnover as a function of light intensity and vesicle composition. The cell doubling time, τ_D, which is inversely proportional to k_{ATP} (Method Details; Hitchcock et al., 2017), is estimated at different light intensities and compared to experimentally determined values to further validate our model.

Light-induced phenotypes of purple phototrophic bacteria are broadly classified into low- and high-light adaptations (Adams and Hunter, 2012; Hitchcock et al., 2017). As the intensity of incident light increases, the number of the RC-LH1, bc_1, and LH2 changes, and the count of vesicles per cell decreases to maintain a steady rate of ATP generation by the chromatophore and, subsequently, the growth and doubling times of the bacteria. When τ is limited by the quinone turnover time of 8 ms (Aird et al., 2007) and $n_{RC} = 24$ (according to our structural model of the chromatophore), k_{ATP} starts saturating at 112 s^{-1} (Figures 6A–6D) for light intensities equal to 1% of full sunlight (Sener et al., 2016). At higher light intensities, this rate slowly increases to 160 s^{-1}. Therefore, our model manifests a low-light adaptation of the chromatophore, which saturates ATP generation under high-light conditions. Because typical illumination levels in the aquatic habitat of purple bacteria can be very low (i.e., about 1%–3% of full sunlight), we find that their photosynthetic machinery is perfectly attuned to work for phenotypes growing under low-light conditions. The computed low-light ATP production rate agrees well with the value of 130 s^{-1} determined by flash-photolysis experiments (Clark et al., 1983). As the light level increases, so does the rate of ATP generation, allowing faster growth and a reduction in the doubling time (Figure 6E). These times decrease and then saturate at higher intensities when the ATP levels plateau. The trend is in excellent agreement with our computations and experimentally determined values. Inability of the bc_1 and RC-LH1 complexes to jointly turn over more than τ^{-1} quinones per second (125 quinones when τ = 8 ms) results in saturation of the ATP yield. Consequently, in a hypothetical chromatophore with three times as many bc_1 complexes, nearly equal to the number of RC-LH1, quinone turnover becomes less rate limiting, and the ATP yield improves to 245 s^{-1} (Figure S7F). However, with such high bc_1 content, an apparently 2-fold more efficient chromatophore will overflow the vesicle with protons at sustained light intensity, reducing the pH and, thus, harming the integrity of the chromatophore membrane and its proteins (Geyer et al., 2010). Put together, the low-light phenotype is suboptimal for ATP yield, due to the 1:3 stoichiometry between the bc_1-to-RC-LH1 complexes. This loss in energy is compensated, nonetheless, by the establishment of a robust electrostatic environment across a small range of pH values (6–7) and broad range of salt conditions (0.15–0.95 M), as observed in our model (Figure 5A). Our spectroscopic experiment confirms that the LH2:LH1 and bc_1:LH1 ratios remain unchanged in fully functional chromatophores within the salinity range of 0.08–0.35 M (Figure 6F). Thus, both computations and experiments establish that the low-light adaptation of the chromatophore remains robust across a wide range of electrostatic environments.

Purple bacteria may encounter salt stress, so we tested our computational model under conditions of low salinity, an environment relevant to the chromatophore under native conditions (Lavergne et al., 2009). At low-salt conditions (0.02 M), when the cyt c_2-mediated electron transfer time, τ , is equal to 71 ms, the kinetic model predicts an ATP yield of 66 s^{-1} (Figure 6D); i.e., about one-third of that under a salt strength of 0.15 M. Nevertheless, when the bc_1-to-RC-LH1 ratio increases in the model from 1:3 to 1:2, the physiological ATP activity is revived, even at low salt strengths. Achieving more bc_1 per RC-LH1 necessitates denser protein packing within the same vesicle volume. This dense arrangement in a bc_1-rich membrane compensates for the loss in the rate of electron transport by enhancing the probability of productive cyt c_2-bc_1 recognition and resurrects a steady ATP yield.

The bc_1-rich model offers clues regarding the functioning of analogous bioenergetic membranes. A dense packing of proteins in the mitochondrion induces the formation of supercomplexes referred to as the respirasome (Letts et al., 2016). Remarkably similar to our model of the bc_1-rich chromatophore, respirasome formation avoids apoptotic low-salt stress toward ATP generation by improving the targetable characteristics of cyt *c*. At 0.15 M salt and beyond, where most experiments are performed, including those reported here, our model demonstrates that dielectric screening is sufficient to ensure targetability of cyt c_2, thus avoiding the need for any RC-bc_1 supercomplex. These conditions

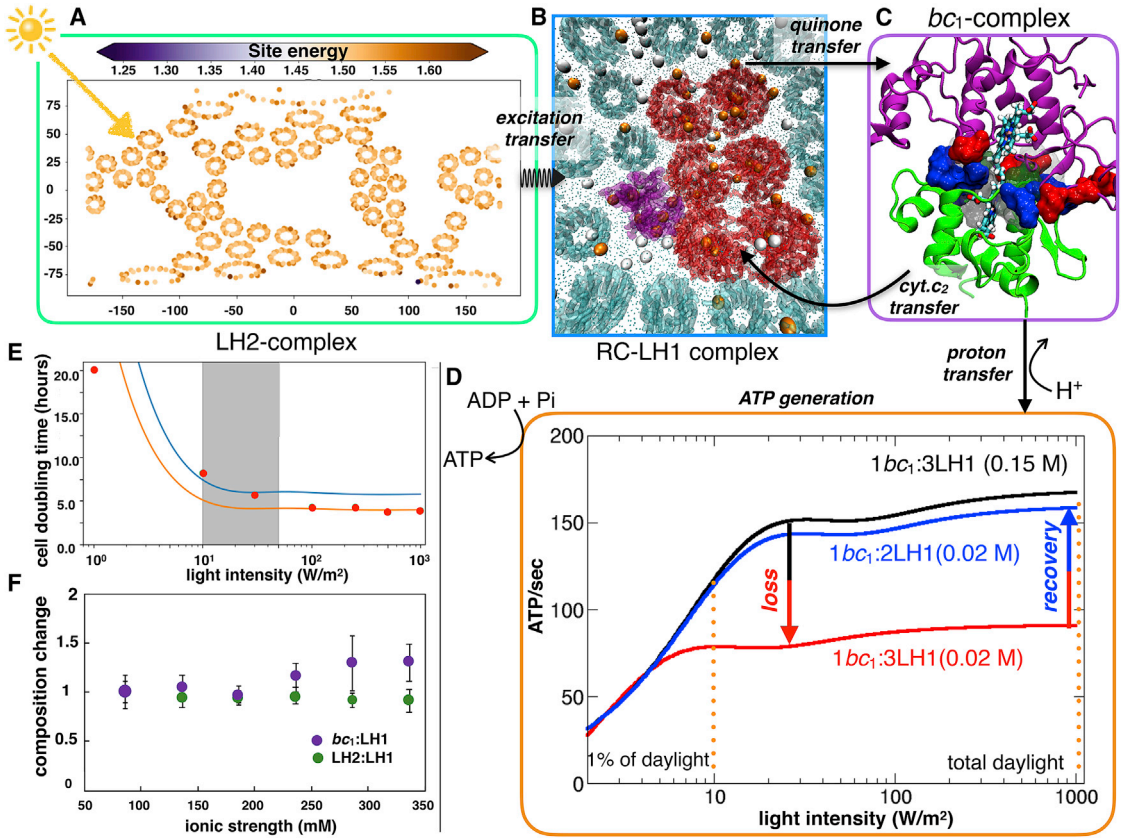

Figure 6. Kinetics Model of ATP Turnover Predicts the Light-Absorption Phenotype of Purple Bacteria

(A) Influence of environment on the average excitation energies of the B800 BChl pigments. The variation in the average excitation energies of B800 among the different LH2 rings because of the thermal disorder captured by the MD simulation was mapped spatially using a 2D Mollweide projection.

(B) Following excitation transfer, charge separation at RC-LH1 releases electrons, transferred by charge carrier quinone molecules to the bc_1 complex. A membrane-wide view of swimming (white) and diving (orange) quinone molecules illustrates that it is more probable for the former to be away from the protein-lipid interface, whereas the latter is significantly close to the protein networks. The diving quinones are stabilized by the positive electrostatic potential in the vicinity of the proteins (Figure S4).

(C) Closing the electron chain, a second carrier, cyt c_2, binds to bc_1, abstracts an electron, and diffuses back to RC-LH1.

(D) Oxidation of the reduced quinone by bc_1 is accompanied by generation of a proton-motive force, driving ATP synthesis. The ATP production rate is presented as a function of incident sunlight intensity, showing saturation under low-light conditions. At low salt strengths, extended cyt c_2 turnover times lower the ATP production rate 2-fold. The model indicates an increase in ATP production when the bc_1:LH1 composition changes from 1:3 to 1:2.

(E) Comparison between experimentally observed cell doubling times (red dots) and those derived from ATP production rates of the simulated chromatophore. The orange line gives cell doubling times when a theoretical maximum of 32 g of dry cell mass is generated per mol of ATP consumed (Russell and Cook 1995). The blue line uses an average dry cell mass of 22 g/mol of ATP value for bacteria (Russell and Cook 1995). The error bars (1 SD) on the experimental data are smaller than the size of the corresponding dots.

(F) Chromatophore compositions as a function of environmental ionic strength, indicating a robust architecture for energy conversion across these conditions. At 0.15 M, the LH2:LH1 ratio is 1:2.6 and that of bc_1:LH1 is 1:3.

have been studied extensively in spectroscopic experiments, which show that (1) the relative bc_1-to-RC-LH1 and LH2-to-RC-LH1 ratios remain unchanged beyond 0.15 M and up to 0.35 M (Figure 6F), and (2) supercomplex formation is absent. Still, our model does not discount the possibility that tighter bc_1-RC-LH1 complexes could form and predicts the correct conditions for tracking them in future experiments.

DISCUSSION

We have developed a comprehensive organelle-scale model that describes the energy conversion processes in purple bacterial photosynthesis and accounts for the cooperation between the constituent proteins in terms of molecular interactions. The entire network of physicochemical events is cast as three mutually coupled reactions: light harvesting, diffusive charge transport, and protein conformational transitions. The rate-determining reactions are identified and simulated in all-atom detail to elucidate how coupling between multiple components of the network tunes the kinetic barrier of the rate-determining steps. We find that the curvature of the chromatophore membrane segregates groups of proteins with distinct functions into separate domains, and thermal disorder of the lipids tunes the efficiency of excitation transfer. The protein conformations support the

creation of an electrostatic environment that enables robust recognition and binding kinetics of quinone and cyt c_2 charge carriers to their targets and a directional electron flow. At larger spatiotemporal scales, the diffusion and binding rates are integrated into a kinetic model that captures the emergence of a phenotype starting from detailed molecular interactions (Hitchcock et al., 2017). We find that the protein composition and density within the chromatophore are optimized to ensure adaptability to a diverse range of environmental conditions, including low light, even at the cost of suboptimal ATP yield. The mechanism responsible for avoiding energy dissipation is broadly applicable to the mitochondrial electron chain.

Our atoms-to-phenotype models enable discovery of biological design principles, the underlying physics of which can extend beyond the system of interest, and predictions of testable phenotypic properties across a broad range of environmental conditions. Indeed, computational simulations of chromatophore energetics, tested across a range of environmental conditions, predict functional robustness under low-light and salt-stressed conditions. The model further brings to the fore new energy-conversion pathways with non-native protein composition.

STAR★METHODS

Detailed methods are provided in the online version of this paper and include the following:

- KEY RESOURCE TABLE
- LEAD CONTACT AND MATERIALS AVAILABILITY
- EXPERIMENTAL MODEL AND SUBJECT DETAILS
- METHOD DETAILS
  - Initial Model
  - MD simulations
  - QM/MM simulations
  - MARTINI simulations
  - Membrane curvature analysis
  - Electrostatic calculations
  - BD simulations
  - Umbrella sampling simulations
  - Diffusion coefficient computation
  - Mean first passage time computation
  - Chromatophore rearrangement
  - Rate kinetics of ATP synthesis
  - Lipid analysis
  - Spectroscopic and growth measurements
  - Modeling of cell doubling times
  - Proposed swimming versus diving quinone experiments
  - Limitations and error propagation in the chromatophore model
  - List of Abbreviations
- QUANTIFICATION AND STATISTICAL ANALYSIS
- DATA AND CODE AVAILABILITY

SUPPLEMENTAL INFORMATION

Supplemental Information can be found online at https://doi.org/10.1016/j.cell.2019.10.021.

ACKNOWLEDGMENTS

A.S. acknowledges start-up award funds from Arizona State University and grants from the Research Corporation for Science Advancement and the Gordon and Betty Moore Foundation; United States, Lightworks Foundation, and Flinn Foundation. E.T., A.A., C.M., A.S., C.C., B.I., I.T., D.C., J.E.S., and J.P. acknowledge NIH grants P41-GM104601 (PI: E.T.) and NIH R01-GM067887 (PI: E.T.). A.S., C.M., Z.L.-S., and A.A. acknowledge the Center for Physics of Living Cells (NSF PHY-1430124). M.S. and Z.L.-S. also acknowledge NSF funding through MCB1616790. T.V.P. acknowledges support from the Department of Chemistry, the School of Chemical Sciences, and the Office of the Vice Chancellor for Research at the University of Illinois at Urbana-Champaign. C.C. acknowledges support from the Contrat Plan État Région (CPER) IT2MP and the European Regional Development Fund (ERDF). Work in D.P.T.'s group is supported by the Natural Sciences and Engineering Research Council (Canada) with further support from the Canada Research Chairs Program and Alberta Innovates Technology Futures. D.P.T. and K.H.D.M. acknowledge Compute Canada, funded by the Canada Foundation of Innovation and partners, for computational resources. U.K. acknowledges grant KL 1299/12-1 from the Deutsche Forschungsgemeinschaft (DFG). D.J.K.S., A.H., and C.N.H. acknowledge research grant BB/M000265/1 from the Biotechnology and Biological Sciences Research Council (UK). C.N.H. was also supported by advanced award 338895 from the European Research Council. The study was also funded by the Photosynthetic Antenna Research Center (PARC), an Energy Frontier Research Center supported by the Department of Energy, Office of Science, and Office of Basic Energy Sciences under award DE-SC0001035 (to C.N.H., K.S., and M.S.). This research used resources of the Oak Ridge Leadership Computing Facility, which is supported by the Office of Science, Department of Energy (DE-AC05-00OR22725).

AUTHOR CONTRIBUTIONS

Conceptualization, A.S., A.A., M.S., C.N.H., and K.S.; Methodology, A.S., M.S., C.M., A.A., U.K., C.C., D.P.T., Z.L.-S., and C.N.H.; Investigation, A.S., C.M., K.H.D.M., D.J.K.S., M.S., U.K., J.W.V., J.N., I.T., D.E.C., A.H., T.V.P., and M.I.M.; Writing – Original Draft, A.S., A.A., K.H.D.M., M.S., C.C., Z.L.-S., E.T., and C.N.H.; Writing – Review & Editing, J.W.V., J.N., A.S., A.A., C.C., K.H.D.M., M.S., U.K., D.P.T., E.T., D.J.K.S., and A.H.; Visualization, B.I., J.E.S., and A.S.; Funding Acquisition, A.S., E.T., Z.L.-S., A.A., and K.S.; Resources, A.S., J.C.P., J.E.S., A.A., Z.L.-S., and E.T.; Supervision, A.S., A.A., C.N.H., D.P.T., and K.S.

DECLARATION OF INTERESTS

The authors declare no competing interests.

Received: March 27, 2019
Revised: September 4, 2019
Accepted: October 21, 2019
Published: November 14, 2019

REFERENCES

Adams, P.G., and Hunter, C.N. (2012). Adaptation of intracytoplasmic membranes to altered light intensity in Rhodobacter sphaeroides. Biochim. Biophys. Acta *1817*, 1616–1627.

Afanasenkau, D., and Offenhäusser, A. (2012). Positively Charged Supported Lipid Bilayers as a Biomimetic Platform for Neuronal Cell Culture. *28*, 13387–13394.

Aird, A., Wrachtrup, J., Schulten, K., and Tietz, C. (2007). Possible pathway for ubiquinone shuttling in Rhodospirillum rubrum revealed by molecular dynamics simulation. Biophys. J. *92*, 23–33.

Allen, J.P. (2017). Design of energy-transducing artificial cells. Proc. Natl. Acad. Sci. USA *114*, 3790–3791.

Anno, T., and Sadô, A. (1958). Electronic states of p-benzoquinone. III. Calculation of the out-of-plane vibrational frequencies in the ground electronic state. Bull. Chem. Soc. Jpn. *31*, 728–733.

Authenrieth, F., Tajkhorshid, E., Schulten, K., and Luthey-Schulten, Z. (2004). Role of water in transient cytochrome c2 docking. J. Phys. Chem. B *108*, 20376–20387.

Bahatyrova, S., Frese, R.N., van der Werf, K.O., Otto, C., Hunter, C.N., and Olsen, J.D. (2004). Flexibility and size heterogeneity of the LH1 light harvesting complex revealed by atomic force microscopy: functional significance for bacterial photosynthesis. J. Biol. Chem. *279*, 21327–21333.

Baker, N.A., Sept, D., Joseph, S., Holst, M.J., and McCammon, J.A. (2001). Electrostatics of nanosystems: application to microtubules and the ribosome. Proc. Natl. Acad. Sci. USA *98*, 10037–10041.

Bazil, J.N., Vinnakota, K.C., Wu, F., and Beard, D.A. (2013). Analysis of the kinetics and bistability of ubiquinol:cytochrome c oxidoreductase. Biophys. J. *105*, 343–355.

Berendsen, H.J.C., van der Spoel, D., and van Drunen, R. (1995). GROMACS: a message-passing parallel molecular dynamics implementation. Comput. Phys. Commun. *91*, 43–56.

Berry, E.A., Guergova-Kuras, M., Huang, L.S., and Crofts, A.R. (2000). Structure and function of cytochrome bc complexes. Annu. Rev. Biochem. *69*, 1005–1075.

Blankenship, R.E. (2014). Molecular Mechanisms of Photosynthesis, Second Edition (John Wiley & Sons, Inc.).

Boyd, K.J., Alder, N.N., and May, E.R. (2017). Buckling under pressure: curvature-based lipid segregation and stability modulation in cardiolipin-containing bilayers. Langmuir. *23*, 6937–6946.

Camargo, C. (2018). Physics makes rules, evolution rolls the dice. Science *361*, 236.

Cartron, M.L., Olsen, J.D., Sener, M., Jackson, P.J., Brindley, A.A., Qian, P., Dickman, M.J., Leggett, G.J., Schulten, K., and Neil Hunter, C. (2014). Integration of energy and electron transfer processes in the photosynthetic membrane of Rhodobacter sphaeroides. Biochim. Biophys. Acta *1837*, 1769–1780.

Chandler, D.E., Hsin, J., Harrison, C.B., Gumbart, J., and Schulten, K. (2008). Intrinsic curvature properties of photosynthetic proteins in chromatophores. Biophys. J. *95*, 2822–2836.

Chandler, D.E., Strümpfer, J., Sener, M., Scheuring, S., and Schulten, K. (2014). Light harvesting by lamellar chromatophores in Rhodospirillum photometricum. Biophys. J. *106*, 2503–2510.

Cheng, Y. (2015). Single-particle cryo-EM at crystallographic resolution. Cell *161*, 450–457.

Clark, A.J., Cotton, N.P.J., and Jackson, J.B. (1983). The relation between membrane ionic current and ATP synthesis in chromatophores from Rhodopseudomonas capsulata. Biochim. Biophys. Acta *723*, 440–453.

Comayras, F., Jungas, C., and Lavergne, J. (2005a). Functional consequences of the organization of the photosynthetic apparatus in Rhodobacter sphaeroides. I. Quinone domains and excitation transfer in chromatophores and reaction center.antenna complexes. J. Biol. Chem. *280*, 11203–11213.

Comayras, F., Jungas, C., and Lavergne, J. (2005b). Functional consequences of the organization of the photosynthetic apparatus in Rhodobacter sphaeroides: II. A study of PufX- membranes. J. Biol. Chem. *280*, 11214–11223.

Comer, J., and Aksimentiev, A. (2012). Predicting the DNA sequence dependence of nanopore ion current using atomic-resolution Brownian dynamics. J. Phys. Chem. C Nanomater Interfaces *116*, 3376–3393.

Corradi, V., Sejdiu, B.I., Messa-Galloso, H., Abdizadeh, H., Noskov, S.Y., Marrink, S.J., and Tieleman, D.P. (2019). Emerging diversity in lipid-protein interactions. Chem. Revi. *119*, 5775–5848.

Crofts, A.R. (2004). The cytochrome bc1 complex: function in the context of structure. Annu. Rev. Physiol. *66*, 689–733.

Culberson, J.C., Knappe, P., Rösch, N., and Zerner, M.C. (1987). An intermediate neglect of differential overlap (INDO) technique for lanthanide complexes: studies on lanthanide halides. Theor. Chim. Acta *71*, 21–39.

Dahlberg, P.D., Ting, P.-C., Massey, S.C., Allodi, M.A., Martin, E.C., Hunter, C.N., and Engel, G.S. (2017). Mapping the ultrafast flow of harvested solar energy in living photosynthetic cells. Nat. Commun. *8* https://doi.org/10.1038/s41467-017-01124-z.

Dashti, A., Shekhar, M.S., Hail, D.B., Mashayekhi, G., Schwander, P., des Georges, A., Frank, J., Singharoy, A., and Ourmazd, A. (2019). Functional pathways of biomolecules retrieved from single-particle snapshots. bioRxiv. https://doi.org/10.1101/291922.

Di Bernardo, S., Fato, R., Casadio, R., Fariselli, P., and Lenaz, G. (1998). A high diffusion coefficient for coenzyme Q10 might be related to a folded structure. FEBS Lett. *426*, 77–80.

Durrant, J.D., and Amaro, R.E. (2014). LipidWrapper: an algorithm for generating large-scale membrane models of arbitrary geometry. PLoS Comput. Biol. *10*, e1003720.

Engstrom, G., Xiao, K., Yu, C., Yu, L., Durham, B., and Millett, F. (2002). Photoinduced electron transfer between the Rieske iron-sulfur protein and cytochrome c(1) in the Rhodobacter sphaeroides cytochrome bc(1) complex. Effects of pH, temperature, and driving force. J. Biol. Chem. *277*, 31072–31078.

Ermak, D.L., and Mccammon, J.A. (1978). Brownian dynamics with hydrodynamic interactions. J. Chem. Phys. *69*, 1352–1360.

Förster, T. (1948). Zwischenmolekulare energiewanderung und fluoreszenz. Ann. Phys. *437*, 55–75.

Frese, R.N., Pàmies, J.C., Olsen, J.D., Bahatyrova, S., van der Weij-de Wit, C.D., Aartsma, T.J., Otto, C., Hunter, C.N., Frenkel, D., and van Grondelle, R. (2008). Protein shape and crowding drive domain formation and curvature in biological membranes. Biophys. J. *94*, 640–647.

Gerencsér, L., Laczkó, G., and Maróti, P. (1999). Unbinding of oxidized cytochrome c from photosynthetic reaction center of Rhodobacter sphaeroides is the bottleneck of fast turnover. Biochemistry *38*, 16866–16875.

Geyer, T., Mol, X., Blass, S., and Helms, V. (2010). Bridging the gap: linking molecular simulations and systemic descriptions of cellular compartments. PLoS ONE *5*, e14070.

Goh, B.C., Hadden, J.A., Bernardi, R.C., Singharoy, A., McGreevy, R., Rudack, T., Cassidy, C.K., and Schulten, K. (2016). Computational methodologies for real-space structural refinement of large macromolecular complexes. Annu. Rev. Biophys. *45*, 253–278.

Green, D.R. (2005). Apoptotic pathways: ten minutes to dead. Cell *121*, 671–674.

Hall, J., Zha, X.H., Durham, B., O'Brien, P., Vieira, B., Davis, D., Okamura, M., and Millett, F. (1987). Reaction of cytochromes c and c2 with the Rhodobacter sphaeroides reaction center involves the heme crevice domain. Biochemistry *26*, 4494–4500.

Hellwig, P. (2015). Infrared spectroscopic markers of quinones in proteins from the respiratory chain. Biochim. Biophys. Acta *1847*, 126–133.

Hitchcock, A., Hunter, C.N., and Sener, M. (2017). Determination of cell doubling times from the return-on-investment time of photosynthetic vesicles based on atomic detail structural models. J. Phys. Chem. B *121*, 3787–3797.

Humphrey, W., Dalke, A., and Schulten, K. (1996). VMD: visual molecular dynamics. J. Mol. Graph. *14*, 33–38, 27–28.

Hsin, J., Gumbart, J., Trabuco, L.G., Villa, E., Qian, P., Hunter, C.N., and Schulten, K. (2009). Protein-induced membrane curvature investigated through molecular dynamics flexible fitting. Biophys. J. *97*, 321–329.

Hunte, C., Solmaz, S., and Lange, C. (2002). Electron transfer between yeast cytochrome $bc_{(1)}$ complex and cytochrome c: a structural analysis. Biochim. Biophys. Acta *1555*, 21–28.

Hunter, C.N., and Turner, G. (1988). Transfer of genes coding for apoproteins of reaction centre and light-harvesting LH1 complexes to Rhodobacter sphaeroides. Microbiology *134*, 1471–1480.

Inbaraj, J.J., Cardon, T.B., Laryukhin, M., Grosser, S.M., and Lorigan, G.A. (2006). Determining the topology of integral membrane peptides using EPR spectroscopy. J. Am. Chem. Soc. *128*, 9549–9554.

Jackson, P.J., Lewis, H.J., Tucker, J.D., Hunter, C.N., and Dickman, M.J. (2012). Quantitative proteomic analysis of intracytoplasmic membrane development in Rhodobacter sphaeroides. Mol. Microbiol. *84*, 1062–1078.

Karplus, M. (2014). Development of Multiscale Models for Complex Chemical Systems: From H+H2 to Biomolecules (Nobel Lecture). Angew. Chem. Int. Ed. *53*, 9992–10005.

Karr, J.R., Sanghvi, J.C., Macklin, D.N., Gutschow, M.V., Jacobs, J.M., Bolival, B., Jr., Assad-Garcia, N., Glass, J.I., and Covert, M.W. (2012). A whole-cell computational model predicts phenotype from genotype. Cell *150*, 389–401.

Kaurola, P., Sharma, V., Vonk, A., Vattulainen, I., and Róg, T. (2016). Distribution and dynamics of quinones in the lipid bilayer mimicking the inner membrane of mitochondria. Biochim. Biophys. Acta *1858*, 2116–2122.

Kimura, Y., Yu, L.J., Hirano, Y., Suzuki, H., and Wang, Z.Y. (2009). Calcium ions are required for the enhanced thermal stability of the light-harvesting-reaction center core complex from thermophilic purple sulfur bacterium *Thermochromatium tepidum*. J. Biol. Chem. *284*, 93–99.

Korte, A., and Farlow, A. (2013). The advantages and limitations of trait analysis with GWAS: a review. Plant Methods *9*, 29.

Kumar, S., Cartron, M.L., Mullin, N., Qian, P., Leggett, G.J., Hunter, C.N., and Hobbs, J.K. (2017). Direct imaging of protein organization in an intact bacterial organelle using high-resolution atomic force microscopy. ACS Nano *11*, 126–133.

Lamichhane, H., Wang, R., and Hastings, G. (2011). Comparison of calculated and experimental FTIR spectra of specifically labeled ubiquinones. Vib. Spectrosc. *55*, 279–286.

Lavergne, J., Verméglio, A., and Joliot, P. (2009). Functional coupling between reaction centers and cytochrome bc1 complexes. In The Purple Phototrophic Bacteria, C.N. Hunter, F. Daldal, M.C. Thurnauer, and J.T. Beatty, eds. (Springer).

Letts, J.A., Fiedorczuk, K., and Sazanov, L.A. (2016). The architecture of respiratory supercomplexes. Nature *537*, 644–648.

Madeo, J., and Gunner, M.R. (2005). Modeling binding kinetics at the Q(A) site in bacterial reaction centers. Biochemistry *44*, 10994–11004.

Marrink, S.J., and Tieleman, D.P. (2013). Perspective on the Martini model. Chem. Soc. Rev. *42*, 6801–6822.

Marrink, S.J., Risselada, H.J., Yefimov, S., Tieleman, D.P., and de Vries, A.H. (2007). The MARTINI force field: coarse grained model for biomolecular simulations. J. Phys. Chem. B *111*, 7812–7824.

Marrink, S.J., Corradi, V., Souza, P.C.T., Ingólfsson, H.I., Tieleman, D.P., and Sansom, M.S.P. (2019). Computational modeling of realistic cell membranes. Chem. Rev. *119*, 6184–6226.

Milano, F., Agostiano, A., Mavelli, F., and Trotta, M. (2003). Kinetics of the quinone binding reaction at the Q_B site of reaction centers from the purple bacteria Rhodobacter sphaeroides reconstituted in liposomes. Eur. J. Biochem. *270*, 4595–4605.

Neese, F. (2018). Software update: the ORCA program system, version 4.0. Wiley Interdiscip. Rev. Comput. Mol. Sci. *8*, e1327.

Noble, J.M., Lubieniecki, J., Savitzky, B.H., Plitzko, J., Engelhardt, H., Baumeister, W., and Kourkoutis, L.F. (2018). Connectivity of centermost chromatophores in Rhodobacter sphaeroides bacteria. Mol. Microbiol. *109*, 812–825.

Novoderezhkin, V.I., and Razjivin, A.P. (1996). The theory of Forster-type migration between clusters of strongly interacting molecules: application to light-harvesting complexes of purple bacteria. Chem. Phys. *211*, 203–214.

Ogren, J.I., Tong, A.L., Gordon, S.C., Chenu, A., Lu, Y., Blankenship, R.E., Cao, J., and Schlau-Cohen, G.S. (2018). Impact of the lipid bilayer on energy transfer kinetics in the photosynthetic protein LH2. Chem. Sci. (Camb.) *9*, 3095–3104.

Olbrich, C., and Kleinekathöfer, U. (2010). Time-dependent atomistic view on the electronic relaxation in light-harvesting system II. J. Phys. Chem. B *114*, 12427–12437.

Olsen, J.D., Tucker, J.D., Timney, J.A., Qian, P., Vassilev, C., and Hunter, C.N. (2008). The organization of LH2 complexes in membranes from Rhodobacter sphaeroides. J. Biol. Chem. *283*, 30772–30779.

Periole, X., Cavalli, M., Marrink, S.J., and Ceruso, M.A. (2009). Combining an elastic network with a coarse-grained molecular force field: structure, dynamics, and intermolecular recognition. J. Chem. Theory Comput. *5*, 2531–2543.

Phillips, J.C., Braun, R., Wang, W., Gumbart, J., Tajkhorshid, E., Villa, E., Chipot, C., Skeel, R.D., Kalé, L., and Schulten, K. (2005). Scalable molecular dynamics with NAMD. J. Comput. Chem. *26*, 1781–1802.

Pingale, S.S., Ware, A.P., and Gadre, S.R. (2018). Unveiling electrostatic portraits of quinones in reduction and protonation states. J. Chem. Sci. *130*, 50.

Pohl, T., Spatzal, T., Aksoyoglu, M., Schleicher, E., Rostas, A.M., Lay, H., Glessner, U., Boudon, C., Hellwig, P., Weber, S., and Friedrich, T. (2010). Spin labeling of the Escherichia coli NADH ubiquinone oxidoreductase (complex I). Biochem. Biophys. Acta *1797*, 1894–1900.

Qian, P., Bullough, P.A., and Hunter, C.N. (2008). Three-dimensional reconstruction of a membrane-bending complex: the RC-LH1-PufX core dimer of Rhodobacter sphaeroides. J. Biol. Chem. *283*, 14002–14011.

Qian, P., Papiz, M.Z., Jackson, P.J., Brindley, A.A., Ng, I.W., Olsen, J.D., Dickman, M.J., Bullough, P.A., and Hunter, C.N. (2013). Three-dimensional structure of the Rhodobacter sphaeroides RC-LH1-PufX complex: dimerization and quinone channels promoted by PufX. Biochemistry *52*, 7575–7585.

Qian, P., Siebert, C.A., Wang, P., Canniffe, D.P., and Hunter, C.N. (2018). Cryo-EM structure of the *Blastochloris viridis* LH1-RC complex at 2.9 Å. Nature *556*, 203–208.

Russell, J.B., and Cook, G.M. (1995). Energetics of bacterial growth: balance of anabolic and catabolic reactions. Microbiol. Rev. *59*, 48–62.

Rust, M.J., Bates, M., and Zhuang, X. (2006). Sub-diffraction-limit imaging by stochastic optical reconstruction microscopy (STORM). Nat. Methods *3*, 793–795.

Sahu, I.D., McCarrick, R.M., and Lorigan, G.A. (2013). Use of electron paramagnetic resonance to solve biochemical problems. Biochemistry *52*, 5967–5984.

Sarewicz, M., Borek, A., Daldal, F., Froncisz, W., and Osyczka, A. (2008). Demonstration of short-lived complexes of cytochrome c with cytochrome bc1 by EPR spectroscopy: implications for the mechanism of interprotein electron transfer. J. Biol. Chem. *283*, 24826–24836.

Sener, M.K., Olsen, J.D., Hunter, C.N., and Schulten, K. (2007). Atomic-level structural and functional model of a bacterial photosynthetic membrane vesicle. Proc. Natl. Acad. Sci. USA *104*, 15723–15728.

Sener, M., Strümpfer, J., Timney, J.A., Freiberg, A., Hunter, C.N., and Schulten, K. (2010). Photosynthetic vesicle architecture and constraints on efficient energy harvesting. Biophys. J. *99*, 67–75.

Sener, M., Strumpfer, J., Singharoy, A., Hunter, C.N., and Schulten, K. (2016). Overall energy conversion efficiency of a photosynthetic vesicle. eLife *5*, e09541.

Singharoy, A., Polavarapu, A., Joshi, H., Baik, M., and Ortoleva, P. (2013). Epitope fluctuations in the human papillomavirus are under dynamic allosteric control: a computational evaluation of a new vaccine design strategy. J. Am. Chem. Soc. *135*, 18458–18468.

Singharoy, A., Barragan, A.M., Thangapandian, S., Tajkhorshid, E., and Schulten, K. (2016). Binding site recognition and docking dynamics of a single electron transport protein: cytochrome c2. J. Am. Chem. Soc. *138*, 12077–12089.

Singharoy, A., Chipot, C., Moradi, M., and Schulten, K. (2017). Chemomechanical coupling in hexameric protein-protein interfaces harnesses energy within V-type ATPases. J. Am. Chem. Soc. *139*, 293–310.

Söderhäll, J.A., and Laaksonen, A. (2001). Molecular dynamics simulations of ubiquinone inside a lipid bilayer. J. Phys. Chem. B *105*, 9308–9315.

Stross, C., Van der Kamp, M.W., Oliver, T.A.A., Harvey, J.N., Linden, N., and Manby, F.R. (2016). How static disorder mimics decoherence in anisotropy

pump-probe experiments on purple-bacteria light harvesting complexes. J. Phys. Chem. B *120*, 11449–11463.

Swainsbury, D.J.K., Martin, E.C., Vasilev, C., Parkes-Loach, P.S., Loach, P.A., and Neil Hunter, C. (2017). Engineering of a calcium-ion binding site into the RC-LH1-PufX complex of *Rhodobacter sphaeroides* to enable ion-dependent spectral red-shifting. Biochim. Biophys. Acta. *1858*, 927–938.

Swainsbury, D.J.K., Proctor, M.S., Hitchcock, A., Cartron, M.L., Qian, P., Martin, E.C., Jackson, P.J., Madsen, J., Armes, S.P., and Hunter, C.N. (2018). Probing the local lipid environment of the Rhodobacter sphaeroides cytochrome bc_1 and Synechocystis sp. PCC 6803 cytochrome b_6f complexes with styrene maleic acid. Biochim. Biophys. Acta. *1859*, 215–225.

Szabo, A., Luthey-Schulten, Z., and Schulten, K. (1980). First passage time approach to diffusion controlled reaction. J. Chem. Phys. *72*, 4350.

Tian, H., Sadoski, R., Zhang, L., Yu, C.A., Yu, L., Durham, B., and Millett, F. (2000). Definition of the interaction domain for cytochrome c on the cytochrome $bc(_1)$ complex. Steady-state and rapid kinetic analysis of electron transfer between cytochrome c and Rhodobacter sphaeroides cytochrome bc(1) surface mutants. J. Biol. Chem. *275*, 9587–9595.

Vasilev, C., Brindley, A.A., Olsen, J.D., Saer, R.G., Beatty, J.T., and Hunter, C.N. (2014). Nano-mechanical mapping of the interactions between surface-bound RC-LH1-PufX core complexes and cytochrome c 2 attached to an AFM probe. Photosynth. Res. *120*, 169–180.

Wells, D.B., Abramkina, V., and Aksimentiev, A. (2007). Exploring transmembrane transport through alpha-hemolysin with grid-steered molecular dynamics. J. Chem. Phys. *127*, 125101.

Wikström, M., Sharma, V., Kaila, V.R.I., Hosler, J.P., and Hummer, G. (2015). New perspectives on proton pumping in cellular respiration. Chem. Rev. *115*, 2196–2221.

Woronowicz, K., and Niederman, R.A. (2010). Proteomic analysis of the developing intracytoplasmic membrane in Rhodobacter sphaeroides during adaptation to low light intensity. Adv. Exp. Med. Biol. *675*, 161–178.

Woronowicz, K., Sha, D., Frese, R.N., and Niederman, R.A. (2011). The accumulation of the light-harvesting 2 complex during remodeling of the Rhodobacter sphaeroides intracytoplasmic membrane results in a slowing of the electron transfer turnover rate of photochemical reaction centers. Biochemistry *50*, 4819–4829.

Xia, D., Esser, L., Tang, W.K., Zhou, F., Zhou, Y., Yu, L., and Yu, C.A. (2013). Structural analysis of cytochrome bc_1 complexes: implications to the mechanism of function. Biochim. Biophys. Acta *1827*, 1278–1294.

Yesylevskyy, S.O., Rivel, T., and Ramseyer, C. (2017). The influence of curvature on the properties of the plasma membrane. Insights from atomistic molecular dynamics simulations. Sci. Rep. *7*, 16078.

Yu, S.P., and Choi, D.W. (2000). Ions, cell volume, and apoptosis. Proc. Natl. Acad. Sci. USA *97*, 9360–9362.

STAR★METHODS

KEY RESOURCE TABLE

REAGENT or RESOURCE	SOURCE	IDENTIFIER
Bacterial and Virus Strains		
Rhodobacter sphaeroides 2.4.1 (wild-type)	S. Kaplan, Department of Microbiology and Molecular Genetics, The University of Texas Medical School, Houston, Texas 77030, USA	N/A
Rhodobacter sphaeroides 2.4.1 (*fbcC*::thrombin-His_{10})	Cartron et al., 2014	N/A
Chemicals, Peptides, and Recombinant Proteins		
n-dodecyl-beta-D-maltopyranoside (DDM)	Anatrace	Cat# D310
Poly(styrene-co-maleic anhydride), 2:1 10 kDa	Polyscope	Cat# Xiran SZ30010
Partsil Diamond TLC plate	Whatman	Discontinued
Phosphatidylcholine	Sigma-Aldrich	Cat# P2772-100MG
Phosphatidylethanolamine	Sigma-Aldrich	Cat# P6386-5MG
Phosphatidylglycerol	Sigma-Aldrich	Cat# P0514-5MG
Osram 116W Halogen Light Bulb	RS-online	Cat# 775-5277
M22+ media	Hunter and Turner 1988	N/A
Casein Hydrolysate (Casamino acids)	Sigma-Aldrich	Cat# 22090-500G
Software and Algorithms		
NAMD	Phillips et al., 2005	http://www.ks.uiuc.edu/Research/namd/
VMD	Humphrey et al., 1996	http://www.ks.uiuc.edu/Research/vmd/
LipidWrapper	Durrant and Amaro, 2014	http://rocce-vm0.ucsd.edu/data/sw/hosted/lipidwrapper/ https://github.com/jvant/Chromatophore_Large_System_Simulation
Gridforces/grid-steered molecular dynamics	Wells et al., 2007	http://bionano.physics.illinois.edu/node/109
ZINDO/S-CIS	Culberson et al., 1987; Olbrich and Kleinekathöfer, 2010	http://link.springer.com/10.1007/BF00538479
ORCA	Neese, 2018	https://orcaforum.kofo.mpg.de/app.php/portal
GROMACS	Berendsen et al., 1995	http://www.gromacs.org
Martini force field	Marrink et al., 2007	http://cgmartini.nl
APBS	Baker et al., 2001	http://www.poissonboltzmann.org
BD	Ermak and Mccammon, 1978	http://aip.scitation.org/doi/10.1063/1.436761
ARBD	Comer and Aksimentiev, 2012	http://bionano.physics.illinois.edu/arbd
BEUS	Singharoy et al., 2016	https://pubs.acs.org/doi/10.1021/jacs.6b01193
Generalized weighted Histogram methodology	Singharoy et al., 2017	https://pubs.acs.org/doi/10.1021/jacs.6b10744
Video S1	This article	https://data.mendeley.com/datasets/hh3kv79k7w/1
Video S2	This article	https://data.mendeley.com/datasets/hh3kv79k7w/1
Video S3	This article	https://data.mendeley.com/datasets/hh3kv79k7w/1

LEAD CONTACT AND MATERIALS AVAILABILITY

Further information and requests for resources or reagents should be directed to and will be fulfilled by the Lead Contact, Abhishek Singharoy (asinghar@asu.edu). This study did not generate new unique reagents.

EXPERIMENTAL MODEL AND SUBJECT DETAILS

The wild-type and *fbcC*::thrombin-His_{10} strains of *Rhodobacter* (*Rba.*) *sphaeroides* 2.4.1 used in this study have been described previously (Cartron et al., 2014). The *fbcC*::thrombin-His_{10} strain produces a His-tagged bc_1 complex.

METHOD DETAILS

Initial Model

The construction of the structural model for the low-light adapted *Rba. sphaeroides* chromatophore employed in this study is based on atomic-force microscopy (AFM), electron microscopy (EM), crystallography, mass spectrometry, proteomics, and optical spectroscopy data, as detailed in Cartron et al. (2014). The supramolecular organization of the chromatophore was determined through assignment protocols for protein positions following based primarily on AFM and EM images (Sener et al., 2007). The stoichiometry of light-harvesting proteins was determined by optical spectroscopy (Sener et al., 2010) and lipid composition was determined by mass spectrometry (Cartron et al., 2014). The inverse-Mollweide transformation was employed to map the planar membrane patches viewed through AFM imaging onto spherical domains, followed by removal of steric clashes and adjusting for the observed packing pattern of constituting proteins. An inner vesicle diameter of approximately 50 nm was employed (Qian et al., 2008). This chromatophore model was found to be robust after more than half a μs of MD simulation performed on the DOE's Titan Supercomputer with NAMD2.12 (Figure S1).

MD simulations

MD is a computer simulation method, which allows the study of biological systems with atomic detail. In a nutshell, this method tracks the physical movement of individual atoms using Newton's laws of motion. By solving Newton's equations, one can generate a trajectory of atoms (and, hence, of molecules), and obtain numerical values of the potential energy and of the interatomic forces acting on the particles.

As summarized in Figure S1, the modeling began with a protein-only structure of the chromatophore vesicle derived from AFM, electron microscopy and mass spectrometric data (Cartron et al., 2014), and MD-equilibrated structures of individual POPC-embedded RC-LH1, LH2 (Chandler et al., 2008), bc_1 (Singharoy et al., 2016) and ATP synthase models (Singharoy et al., 2017). Each protein within the chromatophore scaffold was overlaid with its membrane-embedded counterpart. Then the original protein inside the chromatophore was replaced by the equilibrated model with one ring of lipid around it. To uniformly construct a lipid bilayer on protein-excluded areas of the chromatophore surface, these ring-encased proteins were overlaid with a POPC-only lipid vesicle of radius 30 nm; a 2 Å exclusion radius, employed for the lipid placement around protein-lipid rings, suffices to avoid unfavorable steric interactions between the proteins and the lipids. Use of protein-lipid ring for membrane embedding instead of a protein-only embedding avoided completely the formation of ring-piercing artifacts. Some unfavorable overlap remained due to the inter-twining of the lipid tails. Direct minimization was unable to remove this artifact. The inter-carbon distances in the lipid tail were shrunk till the inter-twining was removed (Tcl script is provided in the Key Resources Table). Thereafter, brute-force energy minimization within NAMD (Phillips et al., 2005) resurrected the length of the lipid tails, but now avoiding the unphysical twining effect.

The resulting vesicle was immersed in a water droplet, wherein the lipid molecules could relax under spherical boundary conditions for a period of 2 ns (0.5 ns with the lipid-head and the proteins constrained to initial position, and the remaining 1.5 ns with just the protein constrained). The partially equilibrated lipids were then heterogenized by randomly mutating the PC-head groups to PG and PE (Chandler et al., 2014) under compositional restraints of 22% POPC, 22% POPG and 56% POPE on the outer (cytoplasmic) side and 24% POPC, 10% POPG and 66% POPE on the inner (periplasmic) side, consistent with lipid measurements in photosynthetic bacterial membranes. In addition, 900 charge-carrier quinone molecules were randomly introduced in the membrane, 600 of uniformly distributed and the other 300 were co-located in the vicinity of the quinone-binding bc_1 and RC-LH1 complexes. Finally, the lipid and quinone-corrected chromatophore model was placed inside a water cube of dimensions 110 nm. All overlapping water molecules within 1.4 Å of the chromatophore vesicle were removed, and the solvated system was ionized to neutrality, constituting a simulation system of size 136 M atoms. An octagonal box is presented here for visualization of the system, as rendering of the complete system is not yet feasible due to hardware limitations.

The chromatophore was constructed, solvated and ionized within a water box of 110 nm^3. Initial MD simulation of the 136 M-atom system developed instabilities within the first ns. These instabilities, manifested as protein and/or lipid-excluded holes on the chromatophore surface, result from a combination of (i) inaccurate number of lipid molecules and (ii) water molecules on either side of the initial chromatophore membrane. Described below, 15 ns and 25 ns of separate constrained MD simulations were performed on NCSA's Blue Waters supercomputer to recover the correct lipid and water density. These simulations leveraged the LipidWrapper (Durrant and Amaro, 2014) and grid forces capabilities of NAMD (Wells et al., 2007). A 500-ns MD simulation ensued on Oak Ridge Leadership Computing Facility's Titan under NPT conditions. A total of 4,096 to 8,192 nodes were employed at a time to run the simulations. All the simulations are summarized in Table 1. Details of the production run, including all simulation parameters are now provided.

The following strategy was employed to decouple the two aforementioned issues and address them sequentially. A grid potential was defined at the resolution of 1 Å about the chromatophore surface, which softly repelled the water away from the surface, while

allowing the protein-lipid and lipid-lipid interactions to equilibrate during short 5 ns NVT simulations. This set-up would allow instabilities in the form of holes on the chromatophore surface only due to insufficient number of lipid molecules; imbalance in the number of water molecules on either side of the membrane will have minimal consequence on the chromatophore stability. The holes were allowed to form and equilibrate, but water passage was negated due to the presence of the grid-potential. LipidWrapper was employed to fix these holes (tcl scripts are provided with the Key Resources Table) through the insertion of filler lipids. After each round of hole-formation, the holes were iteratively filled till LipidWrapper could not identify any new holes. A total of 4 iterations were performed for the number of lipids to converge.

In order to equilibrate the water on either side of the membrane, two RC-LH1 monomers were removed from chromatophore surface, creating a couple of holes on the surface. Lipids within a 5 Å radius about these holes were constrained. The holes would allow passage of water across the membrane, letting the rest of the chromatophore relax without inducing any global instability. In fact, during the modeling phase, the area about the RC-LH1 monomers were found to be most susceptible to instability. Thus, our choice of artificially creating holes in these areas and constraining the vicinity prevents any instability propagation through the membrane. It takes approximately 25 ns for the density of water to converge on either side of the membrane (Figure S1C). Thereafter the missing RC-LH1 monomers were reintroduced into the membrane by excluding some local water molecule, and the long MD simulation was initiated. All the test simulations were performed on NCSA's BlueWaters supercomputer.

All simulations were performed with the MD software NAMD 2.12 using the CHARMM36 force field for proteins and lipids (Phillips et al., 2005). The force field parameters for the photosynthetic cofactors such as chlorophyll and quinone molecules have been obtained from our past studies of the individual proteins (Chandler et al., 2008; Chandler et al., 2014). A configuration file is provided with the Key Resources Table enlisting all the necessary NAMD input arguments employed by the simulation. Some key arguments are mentioned.

Simulations were performed with an integration time step of 1fs where bonded interactions were computed every time step, short-range non-bonded interactions every two timesteps, and long-range electrostatic interactions every four timesteps. A cutoff of 12Å was used for van der Waals and short-range electrostatic interactions: a switching function was started at 10 Å for van der Waals interactions to ensure a smooth cutoff. The simulations were performed under periodic boundary conditions, with full-system, long-range electrostatics calculated by using the PME method with a grid point density of 1 $Å^{-1}$. The unit cell was large enough so that adjacent copies of the system did not interact via short-range interactions. Since the chromatophore dimensions vary between 50 to 60 nm (Figure S1), a water box of 110 nm maintains a padding of ~25 nm on all sides. The systems were kept at constant temperature using Langevin dynamics for all non-hydrogen atoms with a Langevin damping coefficient of $5ps^{-1}$.

For the grid-constrained NVT simulations to correct on-the-fly for the number of lipids employed a Gscale of 0.3, following similar protocol in other large system simulations (Singharoy et al., 2016). The NPT production runs were performed at 1atm using the Nose-Hoover Langevin piston with a period of 100fs and damping timescale of 50fs. Every model derived from an iteration of lipid updates, was minimized for 10000 steps prior to the adding more lipids in the next round; a total of 4 × 10000 = 40000 minimization steps were performed prior to water equilibration.

Following the equilibration of water in the artificially water permeable chromatophore (created by removing two RC-LH1 monomers), these two proteins were reinserted into the equilibrated chromatophore. 5000 more minimizations steps were performed in the vicinity of the LH2 complex, restraining the rest of the chromatophore. Thereafter the long production run ensued.

QM/MM simulations

Based on the equilibrated MD trajectory, QM/MM calculations were employed to obtain an estimate of the static disorder and lipid curvature in the chromatophore. 200 snapshots from a trajectory being 50 ps apart were analyzed (Table 1). The gap between the ground and the Q_y excited state was determined for all 1701 BChls within LH2 rings for each of these snapshots. For this purpose, we employed the ZINDO/S-CIS approach (Zerner's Intermediate Neglect of Differential orbital with parameters for spectroscopic properties combined with the configuration interaction formalism at the single configuration level) using the ORCA package (Neese, 2018) to determine the vertical excitation energies of the individual pigments (Culberson et al., 1987). The optical properties of the BChl molecules are controlled by the π-electron system and thus the molecules were truncated to enhance the computational efficiency. To this end, the phytyl tail as well as all terminal CH_3 and CH_2CH_3 groups were replaced by H atoms. Such truncation schemes have been tested and used previously, e.g., in a study of the LH2 system of *Rhodospirillum molischianum* (Olbrich and Kleinekathöfer, 2010). Importantly, the asymmetric environment of the BChls has been considered using an electrostatic QM/MM coupling scheme with a MM radius of 100 Å, where the MM point charges of all the included residues are considered.

A similar calculation for the chromatophore was repeated for a single LH2 ring based on a separate simulation of 10 ns analyzed every 1 ps. Moreover, due to the nine-fold symmetry of the LH2 system, one only needs to distinguish three pigments in the ideally symmetric case, i.e., one BChl in the B800 ring, and two denoted as α and β in the B850 ring. The fast fluctuations can be extracted reasonably well from simulations of individual rings but for the static disorder one needs to consider, e.g., different protein environments and lipid rearrangements.

MARTINI simulations

In the coarse grained (CG) simulation, the bc_1 complex was embedded in a membrane model representative of the chromatophore composition. The structure of the bc_1 complex was retrieved from the *Protein Data Bank* (PDB), PDB ID 2QJY. Cofactors such as the

hemes and iron-sulfur molecules found in the bc_1 crystal structure were not included in the CG simulation. The composition of the chromatophore membrane consists of an asymmetric distribution of lipids in the cytoplasmic side (upper leaflet: 22% POPG, 22% POPC, 56% POPE) and periplasmic side (lower leaflet: 10% POPG, 24% POPC, 66% POPE), which represents the same lipid composition as found on the full atomistic chromatophore membrane.

CG-MD simulations were carried out under NPT conditions using GROMACS simulation package version 5.1.1 with the Martini v2.2 force field parameters (Marrink et al., 2007), and standard simulation settings. The Martinize script was used to convert the atomistic bc_1 complex to a CG Martini model (Marrink et al., 2007). ElNeDyn elastic network model was applied to particles within a cut-off value of 0.9 nm using a force constant of 500 kJ mol^{-1} nm^{-2} (Marrink et al., 2007) in order to stabilize the protein fold and compensate for the absence of hemes and iron-sulfur molecules. Afterward, the protein was embedded in the chromatophore membrane model using the *Insane* script, preserving the orientation that the protein adopts in the full chromatophore model. The system was solvated using the standard MARTINI water model along with ions set to neutralize the system. The CG system is ca. 21 × 21 nm in the membrane plane (x and y) and contains 57,354 particles in total. The system was simulated for 40 μs of production run with position restraints applied to the backbone beads of the proteins using a force constant of 1 kJ mol^{-1} nm^{-2} (Table 1).

Periodic boundary conditions and semi-isotropic pressure coupling were applied. Energy minimization was performed using 1000 steps of the steepest descent algorithm, followed by equilibration steps, first with position restraints applied to all protein beads, and then to the backbone beads only. The simulation was performed with a 20 fs time step. The temperature at 310 K and pressure 1 bar were maintained during the production run using v-rescale thermostat and Berendsen barostat, respectively, with a time constant for coupling of 1.0 ps for the temperature and 4.0 ps for the pressure. The neighbor list was updated using the Verlet neighbor search algorithm. Non-bonded Coulomb interactions were treated using a reaction-field with a cut-off of 1.1 nm. Lennard-Jones interactions were calculated using a cut-off at 1.1 nm, with the potential shifted to zero at the cut-off using potential-shift-Verlet.

Membrane curvature analysis

Both global as well as local membrane curvature properties of the chromatophore are measured as follows:

Global curvature: A shape-fitting protocol was employed following (Hsin et al., 2009) to capture the curved surface of the membrane. The membrane was first divided into 5 Å × 5 Å vertical square prisms. Position of the phosphate head-groups on the outer/cytoplasmic leaflet within individual prisms were averaged over a window of 5 ns at 0, 250 and 500 ns. A best-fit surface was then computed for the averaged membrane shape through least-squares fitting. The mathematical expression for the best-fit surface is user-defined; for the membrane the patches here, because of their simple overall geometry, a three-dimensional quadratic equation describes their curvature sufficiently well. This equation has the general form:

$$z(x,y) = a + bx + cx^2 + dy + exy + fy^2 \qquad \text{(Equation 1)}$$

Coefficients a, b, c, d, e, and f are free parameters determined during the fitting. Once a best-fit surface in the form of Equation 1 is obtained, radii of curvature can be computed both along the x axis (r_x) and the y axis (r_y) for each point p = (x, y). The radius of curvature along the x axis at point P is computed by measuring the radius of the osculating circle (the circle that has the same curvature as P), passing point P that lies in the x-z plane. The radius of curvature along the y axis, r_y, is defined similarly. Given a surface defined by Equation 1, r_x and r_y can be readily evaluated via the general expressions

$$r_x = \frac{\left[1 + (b + ey + 2cx)^2\right]^{3/2}}{2c}; r_y = \frac{\left[1 + (d + ex + 2fy)^2\right]^{3/2}}{2f} \qquad \text{(Equation 2)}$$

Local curvature: Using simple a trigonometric relationship, the local radius of curvature R of a patch of membrane between two proteins is measured as

$$R = \frac{d}{2sin(\theta_t/2)}, \qquad \text{(Equation 3)}$$

where where h is the height of protein, d is the distance between the centers of two adjacent proteins, θ_t is the tilt angle, and R is the radius of curvature.

Following the relationship Equation 3 between protein tilt-angles (Hsin et al., 2009), the local radius of curvature for LH1-dimer, LH2 and bc_1 complexes are computed to be approximately 22 nm, 17.5 nm and −0.7 nm. Similarity between the radius of curvature induced by light-harvesting complexes of 20-25 nm and the 26.5 nm radius of the modeled chromatophore (Figure S2D) implicates directly protein-lipid interactions of RC-LH1 dimers and LH2 complexes in conforming the membrane to a vesicular shape. As measured by electron microscopy, the RC-LH1 dimers are capable of forming tubular membranes of radius 25-55 nm (Hsin et al., 2009), containing 8-16 dimers per pitch featuring naturally tilt angles of 25-45 degrees as observed in our whole-chromatophore simulations (Figure S2D).

As discussed by Chandler et al. (2008), membrane curving by light harvesting complexes is a manifestation of uneven hydrogen bond formation between the cytoplasmic and periplasmic sides of the bilayer: RC-LH1 dimers form 3 - 4 times more hydrogen bonds on the cytoplasmic side, while LH2 complexes form 2 times more hydrogen bonds (Figures S2A–S2C). Consequently, the RC-LH1

dimers are capable of forming tubular membranes. LH2 complexes however, also require a nearest-neighbor hexametric packing to form pseudo-dimers that characterize similar hydrogen-bond imbalance as the RC-LH1 dimers for inducing curvature (Chandler et al., 2014); loosely-packed LH2 complexes fail to sustain the overall chromatophore curvature. In fact, in the absence of the RC-LH1 dimers and hexagonally-packed LH2 monomers the bc_1-rich chromatophore assumes a flat lamellar shape with loosely spaced light harvesting complexes, thus avoiding thus the formation of any significant membrane curvature.

The bc_1 complex showcases a balanced 1:1 hydrogen bond distribution on either sides of the membrane negating any significant curvature of the adjoining membrane. LH2 complexes in *Rps. acidophila,* which also display an equal number of hydrogen bonds between the cytoplasmic and periplasmic halves of the protein, manifest weaker curvature properties than homologs in *Rb. sphaeroides* (Chandler et al., 2008), in line our rationale of curvature due to uneven hydrogen bond formation.

Conical lipids, such as phosphatidylethanolamine (PE), were found to have little to no significant effect on membrane curvature, consistent with previous studies (Boyd et al., 2017). Another conical lipid, cardiolipin, is expected to release curvature stress and substantiate local flattening around the bc_1 complex. Though cardiolipins have not been incorporated into our chromatophore model, AFM experiments further validate bc_1 localization in flatter regions of the membrane.

The open bc_1 curvature observed in our model has a significant bearing on the mechanism of chromatophore budding from the inner bacterial membrane. It has been suggested that bc_1 complexes form the neck of the vesicle during budding of the chromatophore from the membrane (Frese et al., 2008; Kumar et al., 2017). This hypothesis is further supported by the observation that owing to membrane curvature differences at the neck of the vesicle versus the rest of its surface, the bc_1 complexes remained inaccessible to AFM experiments even when both LH1 and LH2 complexes are observed (Cartron et al., 2014). To this end, our results clearly illustrate that for the lipid composition of bacterial membranes the bc_1 complex exhibit a preference for a particular curvature, which is distinct from LH1 and LH2, and manifests in saddle-shaped neck of the vesicle during budding.

Electrostatic calculations

Frames were selected every 100 ps over the final 250 ns of the MD simulation. There were minimal large-scale structural changes during this part of the trajectory (Figures 2 and S1). Adaptive Poisson Boltzmann Solver or APBS (Baker et al., 2001) computations were performed to solve the nonlinear Poisson Boltzmann equation on each of these frames, using a grid size of 513^3, providing nearly 1 Å resolution to the electrostatic potential maps. Detailed parameters, including input files are provided with the Key Resources Table. Parallel APBS runs were performed employing the comet supercomputer with the big_pb2.py script, also provided with the Key Resources Table. The 2,500 electrostatic potentials were averaged to generate input profiles for the BD simulation. The same procedure was repeated for constructing electrostatic potentials and charge density maps in the range 0 to 0.85 M and pH 4 to 7, to obtain all points shown in Figure 5A.

Finite difference multigrid computations of the electrostatic potential were performed using *mg-para* with the *async* option. 3 processors were employed to compute the potentials along X, Y and Z directions of the system by setting *pdime* to be 3 3 3. An overlap of 10% was employed between meshes on multiple processors. The *cglen* and *fglen* options were chosen to ensure a resolution of 1 Å. A single Debye- Hückel (*sdh*) boundary condition is employed. The dielectric of the chromatophore was set to 2 and that of the solvent was 78.5, and ionic radii were set as per the CHARMM36 force fields. A spline surface model (*spl2*) was used to model the dielectric interface and ion accessibility, and rate of the dielectric transition was set to 0.3. Surface density (*sdens*) was set to 10. Radius of the solvent molecule was set to that of water, namely 1.4 Å. A comparable set of parameters had produced accurate estimation of electrostatic properties in our past studies of virus capsids and photosynthetic proteins.

Analysis of the average electrostatic potential reveals that the effective charge of a chromatophore (a summation of the stationary charges on the surface and those from mobile counter ions in the surroundings) decreases rapidly with an increase in salt strength from 0 to 0.15 M, after which the charge levels at $1x10^{-3}e$ between 0.25 M and 0.95 M (Figure 5A). This decrease in charge can be explained in terms of counter-ion accumulation, screening the surface charges. At 0 M salinity, counter-ion screening is absent. Increasing the salinity to 0.15 M, the counter ions accumulate almost exponentially (Figure 5A), consistent with the solution of PB equations for nanoscale systems, thereby reducing the effective chromatophore charge rapidly. Beyond 0.15 M, when counter-ion accumulation saturates, the effective charge varies linearly with the potential (also see Video S2). The effective charge of the chromatophore decreases slowly between 0.15 and 0.95 M. As a function of pH, the charge rises between pH 4 to 6 before plateauing after pH 7. Under low-pH conditions the acidic side chains lining the cyt c_2-binding surfaces of the bc_1 and RC-LH1 complexes (Figure S7E) remain protonated, alleviating the overall chromatophore charge. Deprotonation of these residues at relatively higher pH values enhances the surface charge, hence, facilitating recognition by the basic residues on cyt c_2's binding surface.

BD simulations

Brownian dynamics simulations were used to monitor the motions of quinone and cyt c_2 molecules on the timescale of hundreds of microseconds. All BD simulations were performed using an in-house-developed GPU-accelerated Brownian dynamics simulation code, Atom Resolved Brownian Dynamics (ARBD) (Comer and Aksimentiev, 2012).

A 2.8 ms simulation of 5,000 independent quinone molecules moving through an idealized representation of the lipid bilayer of the chromatophore permitted the estimation of the lower-bound diffusion-limited timescale of quinone cycling. Each quinone molecule was treated as an isotropic point-like particle with a diffusion coefficient of 7.7×10^{-8} cm^2 s^{-1} (representative of slow swimming quinone derived from Figures 4 and S4A). Interactions between quinone molecules were neglected and the chromatophore was

represented using a rotationally isotropic potential derived using Boltzmann inversion from the radially- and temporally-averaged distribution of the centers of mass of quinone particles observed in all-atom simulation of the chromatophore. The temperature was set to 300 K during the simulation, and integration of the coordinates was performed using a 1 ps timestep. The coordinates of the quinone molecules were written every 10 ns for subsequent analysis described in Figure S4C.

BD simulations of cyt c_2 were performed over a cumulative time of 30 ms under six different conditions, namely (1) pH 4 and 0.02 M salinity, (2) pH 7 and 0.15 M salinity, and (3) pH 7 and 0.25 M salinity, for both the reduced and oxidized chromatophore. These simulation conditions exemplify the micro-environmental stresses that single-electron transfer proteins overcome while shuttling charges across a bioenergetic membrane. For each condition, 500 independent 10 μs trajectories were generated with a single cyt c_2 molecule starting at the center of the chromatophore. Thus, a total of $6 \times 5ms = 30$ ms of BD simulations have been performed (Table 1).

The cyt c_2 molecules were modeled as rigid body particles. At each timestep, a torque and force were evaluated based on the configuration of the system, allowing the update of position and orientation for the rigid body using a symplectic integrator. The mass and moments of inertia of cyt c_2 were calculated directly from the atomic coordinates. The program Hydropro was used to estimate the diagonal components of the diffusion tensor from the atomic coordinates by replacing each surface atom with a sphere subject to Stokes drag. The diffusion tensor was then transformed to translational and rotational friction coefficients according to the Stokes–Einstein relation. These provided Langevin forces and torques at each timestep that kept the system at 300 K. The Lennard-Jones parameters of the atoms comprising the cyt c_2 were clustered into three categories: one representing all Hydrogen atoms, another representing Oxygen and Nitrogen atoms, and the final representing Carbon and Sulfur atoms. The atoms in each category were assigned an average value for the parameters R_{min} and ε, which were used to calculate a potential for the interaction of such an atom with the entire chromatophore using the Implicit Ligand Sampling feature of VMD at 1 Å resolution. The potentials, both electrostatic and Lennard–Jones, were smoothed by a 1 Å wide 3D Gaussian filter to remove noise. These potentials and the corresponding densities were used to perform five hundred 10 μs simulations with cyt c_2 initially placed at the center of the chromatophore. A 100 fs timestep was used and the cyt c_2 coordinates were recorded every nanosecond for subsequent analysis. To obtain transition times and overall affinity, the cyt c_2 and any given chromatophore membrane protein were considered to be in contact after any pair of non-hydrogen atoms from the two proteins came within 7 Å of one another. The contact was considered lost once no pair of atoms from the proteins was found within 16 Å. Contact with the lipid bilayer was similarly defined, except that contacts with the lipid bilayer were not tracked on a per-molecule basis. Similarly, for the quinone carriers, the limiting mean first passage time of diffusion is defined to be the amount of time taken by a quinone molecule to be within 7 Å of RC-LH1 after moving at least 16 Å away from its initial position.

The force and torque on the rigid body due to the chromatophore was calculated as follows. First, a grid of electric charge and Lennard-Jones particle densities were obtained from the atomic coordinates of cyt c_2 with 1 Å resolution. The density in each grid cell experienced a local force due to the corresponding grid-specified chromatophore potential (electrostatic or one of three Lennard-Jones terms). These local forces, and the corresponding torques, were summed over to obtain the total force and torque on the molecule. As mentioned in the previous section, the electrostatic chromatophore potential was obtained from the atomic model with partial charges assigned according the CHARMM36 force-field using the APBS at the relevant ion concentration with 513 grid points in each Cartesian direction (~1 Å resolution).

As depicted in Figure 5B and in the Supporting Animation (Video S3), in all six cases the cyt c_2 protein can be observed to diffuse around the center of the chromatophore until it approaches its surface, whereupon it interacts with proteins or lipid patches. Once near the surface, the majority of the trajectories reveal that the cyt c_2 molecules visited numerous proteins (Figure S5A), transiently binding to them, and diffusing either slowly along the chromatophore surface, or quicker through the solvent. Irrespective of the salinity, both overall targeting and binding efficiency appear to be enhanced under reducing conditions for the chromatophore. The weaker RC-LH1 complex recognition of cyt c_2 under oxidizing conditions, relative to that of bc_1 under reducing conditions, is compensated by a larger number of RC-LH1 complexes than bc_1 complexes. Altogether, our BD simulations demonstrate that the dynamics of cyt c_2 is regulated by the redox state and salinity of the chromatophore. Under native conditions, the electrostatic environment of the vesicle favors directional single-electron transfer from the bc_1 complex to the RC-LH1 complex, and avoids hijack of the charge carrier cyt c_2 protein by anionic lipids on the membrane surface.

Umbrella sampling simulations

Bias-exchange umbrella sampling (BEUS) simulations were performed along the lowest non-equilibrium work path derived from steered MD (SMD) trajectories of cyt c_2 dissociation from bc_1 and RC. Details of these steering simulation have been published separately (Singharoy et al., 2016). Altogether twenty SMD simulations (five for bc_1red-$c_2$ox and bc_1ox-$c_2$red states, respectively before and after electron transfer, and similarly for RCox-$c_2$red and RCred-$c_2$ox) were performed, each for 50 ns with a 1 fs integration time step and a force constant of 5 kcal mol^{-1} Å^{-2}. The lowest work trajectory, namely one where the non-equilibrium work value converged to < 50 kcal mol^{-1} (Figure S7C) was refined with BEUS simulations.

The BEUS simulations for both the bc_1red-$c_2$ox and bc_1ox-$c_2$red states pathways are performed employing the inter-heme CBC distance as the collective variable. To ensure sufficient window overlap in BEUS simulations, the number of 34 windows employed were employed along the dissociation path. An exchange is attempted every 1 ps between each image and one of its two nearest neighboring images in an alternating fashion. Ten replicas per image are employed for 10 ns long BEUS simulations. A force constant of 5 kcal mol^{-1} Å^{-2} is employed to restrain geometrically the position of the umbrellas along the inter-heme distance axis. This protocol resulted in results in roughly similar rate of exchange rates between neighboring windows (ranging from 29% to 40%).

$5 \times 10 replica/window \times 34 window \times 10 ns/replica = 17\ \mu s$ of BEUS simulations were performed for the construction of five one-dimensional free–energy profiles (Table 1). Thereafter our generalized weighted histogram methodology (Singharoy et al., 2017) was employed to re-weight the ensemble and determine the potential of mean force (PMF) profiles (Figures S7A and S7B). Introducing the free-energy profiles in the Szabo-Schulten equation yields a bc_1 and RC association time of cyt c_2 equal to, respectively, 50 ns and 180 ns at 0.15 M salinity, which is comparable to the timescale extracted from the BD simulations.

In the BEUS scheme, samples generated by each umbrella are assumed to satisfy the detailed balance relation and have the correct (biased) Boltzmann distribution. However, the initial conformations are not always selected from the correct distribution. The timescale associated with relaxation of these conformations to a correct distribution, τ, is roughly estimated in ps, employing the relationship $\tau = (M^2 + 1)/10r$ (Singharoy et al., 2017), where M is the number of images in the string and r is the average exchange rate; here, $\tau = 38$ ps, when r is roughly $0.33 ps^{-1}$. Thus, a sample size of 100∼ns/image (10∼ns/replica), which is an order of magnitude more than the relaxation time, is expected to provide a correct biased Boltzmann distribution for the restrained-ensemble.

Convergence of the free-energy calculation is tested for each of the three cases using a resampling protocol. 50% of the data is randomly chosen and two one-dimensional free energy profiles are constructed employing the aforementioned weighted histogram method. The process is repeated 100 times to obtain a collection of 200 PMFs. After these 100 trials a converged mean profile is obtained across the 200 PMFs, and the standard deviation is considered as the error estimate. An error bound of ± 1.5 kcal mol^{-1} is estimated for our PMF calculations (Figures S7A and S7B).

Diffusion coefficient computation

The lateral diffusion coefficient D has been evaluated using the mean square displacement (MSD) relation:

$$\left\langle |r(t) - r(0)|^2 \right\rangle = 6Dt \qquad \text{(Equation 4)}$$

where the mean square displacement of the mass center of the molecule $|\Delta \mathbf{r}(t)|^2$ is calculated from the trajectory. The obtained function converged at $t \geq 4$ ns (Figure S4A), but at longer times, the MSD is based on too few separate events in time. Hence, the interval used to calculate the average of D is chosen from the convergence criteria of Equation 4, giving the lower limit at $t = 4$ ns.

Mean first passage time computation

The Szabo-Schulten-Schulten relationship for determination of rates (k) states (Szabo et al., 1980):

$$k^{-1} = \sum_{I=i}^{n} \left\{ D(x_i) \frac{e^{-\beta F(x_I)}}{\sum_{j=i}^{I} e^{-\beta F(x_j)}} \right\}^{-1}, \qquad \text{(Equation 5)}$$

where the one-dimensional space in x is discretized into I points ranging from $i, \cdots, j \cdots, n$, and $D(x_i)$ and $F(x_i)$ represent, respectively, the diffusivity and the free energy position x_i. Employing the PMF of quinone dynamics derived within the chromatophore membrane (Figure 4B), and the diffusion coefficient of the quinones derived from the MSD method (Figure S4A), the interconversion time from swimming to diving is found to be about 220 ns. Similarly, the PMF of cyt c_2 dissociation derived from BEUS simulations (Figures S7A and S7B) together with diffusion coefficient of 1.080×10^{-6} cm^2 s^{-1} derived by Hydropro, the rate of cyt c_2 binding/unbinding is determined in Figure S7D.

Chromatophore rearrangement

The model has been updated by introducing rearrangements to the original chromatophore structure. Such rearrangements include changing the order and grouping of the RC-LH1 complexes. The original model contained two groupings of three RC-LH1 dimers and two lone RC-LH1 dimers. The new ''shuffled'' model consists of a grouping of four RC-LH1 dimers and a grouping of three RC-LH1 dimers, as well as one lone dimer. Both of these dimer arrangements are inspired from atomic-force microscopy (AFM) experiments (Chandler et al., 2014; Cartron et al., 2014). Adaptive Poisson-Boltzmann solver (APBS) computations of the electrostatic potential were repeated at pH 7 and 0.15 M ionic strength, and the BD simulations of 500 copies of cyt c_2 were performed for 10 μs (similar to the original setting in Table 1). The fraction of time cyt c_2 interacted with its target protein complexes (namely RC-LH1 and bc_1) remains comparable to that of the original model. This finding allows us to ascertain that our model and the discoveries made with it are robust to initial conditions. The nonproductive lipid binding is enhanced in the shuffled or rearranged chromatophore model, implying further that the original model provides a more reasonable description of the through-solvent charge transfer. Since one of the rate-determining steps is the millisecond-scale cyt c_2 binding (Figure S7), and not its microsecond-scale diffusion (Figure S5), and since both models depict comparable cyt c_2 diffusion times (Figure S6), the overall ATP yield will remain unaffected by the alternative RC-LH1 locations within the membrane vesicle.

Rate kinetics of ATP synthesis

Energy conversion steps in the chromatophore from light absorption to ATP conversion are modeled according to the rate kinetics framework introduced in (Sener et al., 2016). Below a summary of this framework is provided in deriving the expression for the

chrometophore-wide ATP synthesis rate, $k_{ATP}(I)$, as a function of incident light intensity, I, given in units of photons absorbed per second for the entire vesicle, under the assumption of steady state illumination.

Energy conversion in the chromatophore are considered in three steps: (i) light harvesting and charge separation, converting quinone into quinol at a RC; (ii) diffusion of charge carriers (quinone/quinol in the membrane and cyt c_2 in the vesicle interior) resulting in the generation of a proton gradient at the cytbc_1; (iii) conversion of ADP into ATP at the ATP synthase upon utilization of the proton gradient.

The efficiency of the first energy conversion step is the so-called quantum yield, q, computed in an effective Hamiltonian framework (Sener et al., 2007, 2010, 2016) based on the generalized Förster formalism (Förster 1948; Novoderezhkin and Razjivin, 1996). The dependence of the quantum yield on the vesicle composition is treated in Sener et al. (2016) as an interpolation between the values for q computed for low light-growth and high light-growth chromatphore stoichiometries, namely, $q = 0.91 + 0.0152(s_0 - s)$, where s is the LH2:RC stoichiometry and s_0 = 2.625 represents the reference vesicle employed in this study (See Supplementary Material of Sener et al., 2016, for details of the corresponding effective Hamiltonian and the computation of the quantum yield.).

The second energy conversion step is characterized by the cycling time, $\tau_{RC}(I)$, of quinones at the RC. This cycling time is established to be rate limiting for energy conversion into ATP under steady state illumination for typical physiological conditions of the chromatophore (Geyer et al., 2010). The cycling time is estimated from the high light and low light limits of $\tau_{RC}(I)$, τ_H and τ_L, respectively, based on experimental observations (Woronowicz et al., 2011), namely,

$$\tau_{RC}(I) = \tau_L + (\tau_H - \tau_L)\left(1 - e^{\frac{1}{2}IqB^{-1}}\right), \qquad \text{(Equation 6)}$$

where $B = 2 \times n_B \tau_B$ is the total turnover capacity of bc_1s, n_B is the number of bc_1 dimers in the chromatophore, and τ_B is the quinone turnover time at a bc_1 (Crofts, 2004).

The third energy conversion step is governed by the ATP synthesis rate, $k_{ATP}(I)$, which, in turn, is expressed in terms of the quinol → quinone turnover rate, $k_{QH2 \rightarrow Q}(I)$, at the cytbc_1, namely, $k_{ATP}(I) = k_{QH2 \rightarrow Q}(I)$. This equality follows from assuming a 12-subunit c-ring for the ATP synthase, in the case of which the so-called Q-cycle admits (Crofts, 2004), for each quinol passage, the release of four protons into the vesicle interior (two at bc_1 and two at RC), i.e., the same number of protons needed for producing one ATP molecule at the ATP synthase. Thus, the ATP synthesis in the chromatophore can be expressed in terms of the quinol turnover processes from the second energy conversion step above. The ATP turnover rate is derived as

$$k_{ATP}(I) = \frac{1}{2} Iq \left(1 + \frac{1}{2} Iq \tau_{RC}(I) \frac{1}{n_{RC}}\right), \qquad \text{(Equation 7)}$$

where n_{RC} is the number of reaction centers. The cycling time, $\tau_{RC}(I)$, corresponds to a chromatophore-wide average and does not incorporate spatial inhomogeneities in the membrane.

Equations 6 and 7 together permit the computation of the ATP turnover rate of the entire chromatophore as a function of incident light intensity for steady state illumination conditions.

Lipid analysis

The bc_1 styrene-maleic acid lipid particles (SMALPs) and chromatophores were prepared from *fbcC*::thrombin-His_{10} *Rba. sphaeroides* (Cartron et al., 2014) and analyzed by thin layer chromatography (TLC) and phosphate quantification as previously described (Swainsbury et al., 2018), with the exception that lipid band intensities were plotted as a fraction of the total.

Spectroscopic and growth measurements

Wild-type *Rba. sphaeroides* 2.4.1 cells were used to inoculate 1 L M22+ medium (Hunter and Turner, 1988) supplemented with 0.1% (w/v) Casamino acids and 0, 50, 100, 150 or 200 mM NaCl. Cells were grown under 30 μmol m^{-2} s^{-1} illumination from Orsam Classic 116W halogen bulbs for 48 hr at room temperature (~21°C). Cells were harvested at 4000 RCF (avg) for 30 min and pellets were suspended in ~10 mL 20 mM Tris pH 8 per gram of wet cell mass and a few crystals of DNase I and Lysozyme (Sigma-Aldrich) were added. Cells were broken by two passages through a French pressure cell (AmInCo, USA) at 20,000 PSI and insoluble debris was removed by centrifugation at 18,459 RCF (avg) for 15 min. Membranes were prepared by layering clarified cell lysate above 40/15% (w/v) sucrose step gradients followed by centrifugation at 57,031 RCF (avg) for 10 hr at 4°C followed by harvesting of the membrane band from the 40/15% interface.

The RC-LH1, LH2 and cytbc_1 content was estimated as described in Swainsbury et al. (2018). Briefly, membranes were diluted to an optical density at 850 nm of 5 in 20 mM Tris pH 8 and spectra were collected in a 4 mm path length cuvette. Spectra were deconvoluted by fitting spectra of pure RC-LH1 and LH2 and a scatter curve to estimate the concentrations of RC-LH1 and LH2 in the samples (see Swainsbury et al., 2017 for a detailed description). Next, spectra were collected in a 1 cm path length cuvette before and after the addition of a few grains of dithionite generating oxidized and reduced spectra. The cytbc_1 content was estimated from reduced minus oxidized difference spectra using extinction coefficients $\varepsilon_{561-575}$ of 22 mM^{-1} cm^{-1} and $\varepsilon_{551-540}$ of 19 mM^{-1} cm^{-1}, for *b*- and *c*-type heme, respectively.

Determination of the cell doubling time of wild-type *Rba. sphaeroides* 2.4.1 grown at different light intensities was reported previously (Hitchcock et al., 2017). Briefly, photosynthetic growth under anaerobic conditions was performed in M22+ medium supplemented with 0.1% (w/v) Casamino acids in completely full and sealed 17 mL sterile glass tubes (~1 cm across). Cultures were inoculated to a starting optical density at 680 nm (OD_{680}) of ~0.05 and incubated at room temperature under a range of light intensities from 1-1,000 Wm^{-2} with mixing to minimize cell shading. Growth was measured by monitoring the OD_{680}. The BChl concentration was determined spectroscopically and used to estimate the number of chromatophores per cell as described previously (Adams and Hunter, 2012; Hitchcock et al., 2017).

Modeling of cell doubling times

Cell-doubling times can be measured experimentally and calculated as a function of illumination, as done in Hitchcock et al., 2017. Comparing experimentally collected data to the rate-kinetic model presented here attests the validity of our model and the discoveries made using this model. The equation below supplies the aforementioned relationship between cell-doubling times and illumination,

$$\tau_D(I) = \frac{M_{cell}(I)/Y_{ATP}}{N_{chrom}(I)\tilde{k}_{ATP}(I)} \quad \text{(Equation 8)}$$

Here, τ_D specifies the cell-doubling time in hours. N_{chrom} is the number of chromatophore vesicles in the cell, which is itself a function of illumination (I). $N_{chrom}(I)$ is determined using a Gaussian process regression directly from the vesicle counts obtained from whole cell spectra (Figures S7G and S7H) in the illumination range of 0.1 to 1000 Wm^{-2} (method detailed in Hitchcock et al., 2017). M_{cell} is simply a function of N_{chrom} multiplied by the weight of a chromatophore added to a constant dry mass of the non-chromatophore parts of the cell. Y_{ATP} or the ATP yield (i.e., the dry mass of a chromatophore generated per mole of ATP) is presented at two values in the main text: 32 g/mol corresponds to the theoretical maximum, while 22 g/mol is the upper echelon of experimentally derived ATP yield values for bacteria (Russell and Cook 1995). $\tilde{k}_{ATP}$ is calculated from our chromatophore model using the rate-kinetic model for energy turnover. As seen in Figure 6E, the $\tilde{k}_{ATP}$ values obtained from the chromatophore model, when inserted into the τ_D equation, give cell-doubling times commensurate to those determined experimentally.

Proposed swimming versus diving quinone experiments

MD simulations of quinone diffusion within a membrane have been reported in the main text. The results of these simulations present two distinct modes of quinone diffusion in the membrane: swimming and diving. The primary distinguishing factor between swimming and diving quinones is the placement of the aromatic headgroups of the quinones with respect to the lipid bilayer. Swimming quinones are typically found in environments that are more enriched in lipid head-groups and water, away from protein complexes, while diving quinones are found in the midplane of the membrane, closer to the protein complexes (Söderhäll and Laaksonen 2001). These two modes of diffusion are observed computationally, opening new possibilities for validation. The potential experiments, though conceptually feasible, requires work that largely goes beyond the scope of the current manuscript.

Fourier transform infrared spectroscopy (FTIR) is a common method for studying the structural changes in quinones in respiratory systems, according to Hellwig 2014. FTIR allows vibrational modes of a single functional group to be observed within a protein, containing 100 or more residues. Data is collected by averaging a large number of scans resulting from several reactions. Analysis of the data will provide vibrational modes of reactants, intermediates, and product states of the reaction. In order to identify specific groups involved in vibrational motions, isotopic substitution is typically used. The first use of this method to study vibrational modes of quinones can be traced back to 1958 (Anno and Sadô, 1958). A significant amount of studies has since been published, improving this method, now allowing different types of quinones to be compared. FTIR can be used to determine distinct conformations of quinones, with the help of stable isotope labeling.

One of the most commonly used stable isotope labels is ^{13}C. We hypothesize that the IR spectrum of a labeled $^{13}C_4$ carbon in ubiquinone, for example, a peak at 1638 cm^{-1} ($13C_4$) and 1648 cm^{-1} (unlabeled) would be observed in solution (Lamichhane et al., 2011) for the swimming quinone. In contrast, the diving quinone will manifest significant red-shifts in the IR spectrum of the labeled C_4 and also C_1 on the aromatic ring of the quinone headgroup. To artificially enhance the difference in the spectra of the swimming and diving quinones, a positively charged lipid, such as 1,2-dioleoyl-3-trimethylammonium-propane (DOTAP), can be added to the assay, such as liposomes (Afanasenkau and Offenhäusser 2012). DOTAP addition will decrease the number of diving quinones, thereby increasing the signal of the swimming ones, further differentiating between the two modes of diffusion.

Similar to the work on mitochondrial complex I, a decyl-ubiquinone derivative with a spin-labeled headgroup can be prepared (Pohl et al., 2010). When immersed within the membrane, the chemical shift of the nitroxylated or methanethiosulfonated quinone headgroup will differ from that when the label is in solution (Sahu et al., 2013). This exact analogy has been used to determine quinone binding pockets in lipid-embedded systems as well the orientation of transmembrane helices in ion channels (Inbaraj et al., 2006). To enhance the strength of the chemical shifts in a swimming versus diving quinone, the membrane itself can be enriched with spin-labeled phospholipids (Sahu et al., 2013). Altered spin-spin coupling between the labeled membrane and the two different kinds of quinones will also provide a statistically significant difference in the signals of swimming and diving species.

The swimming and diving modes of diffusion may also be studied through structural-biology methods, such as cryo-electron microscopy (cryo-EM). Some of the major lipids in photosynthetic membranes are monogalactosyldiacylglycerol (MGDG), digalactosyldiacyl-glycerol (DGDG) and sulfoquinovosyldiacylglycerol (SQDG), and the phospholipid phospha-tidylglycerol (PG), all of which are negatively charged. In the presence of negatively charged lipids, diffusion of the quinones seem to obey the diving mechanism (Figures 4, S4A, and S4B). If the PC-head groups were mutated to a positively charged lipid, such as DOTAP, chances are that the quinones would not dive toward their binding pockets within the membrane. Instead, one would be able to observe more quinones swimming via cryo-EM densities (Qian et al., 2018). Using our latest machine-learning techniques, multiple modes of binding can be directly extracted from two-dimensional cryo-EM images (Dashti et al., 2019).

Limitations and error propagation in the chromatophore model

The chromatophore model offers a multiscale description of the bioenergetic processes across a 30-35 nm radius vesicular membrane. MD simulations have reached the length and accuracy that makes this model tractable. Nonetheless, recognizing the approximations that underlie MD, the reported simulations are all driven by or linked to experimental results, which provide both necessary input and validation. Several of the limitations and their remediations are now outlined.

1. There is no unique structure for an organelle, but the overall size, relative protein arrangements and protein-lipid compositions remain conserved (Marrink et al., 2019), underpinning the construction of a representative model. Similar to traditional electron microscopy experiments, which derive ensemble-averaged representations of a biological object, we use physics-based modeling to integrate all the available data, leading to representative all-atom structures consistent with the data.

In constructing the model, the structures of individual proteins have been derived either from X-ray crystallography or cryo-EM. The experimental resolutions of these models are 2.9Å, 2.0Å, 2.4Å (RC-LH1-PufX dimer (PDB: 6ET5), LH2 (PDB: 1NKZ) and bc_1 (PDB: 2QJY), respectively). Given this high resolution, positions of the individual amino-acid residues and the cofactors are determined unambiguously. The inter-protein distances determined from AFM are known with an uncertainty of 8 Å (Cartron et al., 2014). Nonetheless, the hexameric or pentameric relative arrangements of the light-harvesting proteins are highly reproducible, also validated by similar independent experiments (Chandler et al., 2014). Noting that inter-protein arrangements are accurately determined, and uncertainties in the inter-protein distances are less than 10% that of the overall radius of curvature of 200 Å, such uncertainties have minimal consequence on the overall size and architecture of the modeled chromatophore. Electron tomography already reveals that the size of 53 ± 6 nm is well within the most probable distribution of chromatophore sizes. The error bounds on quantitative mass spectrometry is 0.1–0.7 mole, implying that the mass of the proteins and lipids were determined to within a 10%–20% uncertainty (Cartron et al., 2014; Olsen et al., 2008). Translating these masses into the number of proteins and lipid molecules, we estimate the uncertainty in the number of proteins to be 63 ± 14 light-harvesting LH2 complexes, 11 ± 4 dimeric and 2 monomeric RC-LH1 complexes, 4 ± 1 cytochrome *bc*1 complex dimers, and 2 ± 0.2 ATP synthases and that for lipids to be 16000, within errors of ± 2,500. We have 82 proteins (63 LH2, 11 dimeric and 2 monomeric RC-LH1, 4 bc_1, and 2 ATP synthases) and 17,200 lipids in the computational model, both well within the experimental error.

2. MD simulations over the 500-ns timescale is fraught with a number of assumptions. The first major assumption is that of a model bias. Our model that is found to be stable for microseconds, which, indeed, implies that we are at a local energy minimum, is assumed to be stable across the second- to minute-lifetime of the chromatophore. Since our predicted cell-doubling times based on this atomic model are now experimentally verified, this first assumption appears justified. Our model does not capture protein diffusion through the membrane; it does capture, however, charge-carrier diffusion through the membrane or the solvent. The binding-unbinding events that determine the ATP-turnover occur on a timescale faster than protein diffusion through the membrane. Thus, assuming the membrane-embedded proteins to be quasi-static leads to ATP yield and cell-doubling time values that are quantitatively accurate.
3. Normally, polarizability of the medium plays a key role in membrane biophysics of the cells. Since our model builds on static charges that do not partake in any explicit bond forming or breaking events, the impact of polarizability is greatly simplified. In favor of this assumption is the observation that chemical reactions are often not rate-determining. It is rather the conformational transition and diffusive events that classical energy functions or force fields capture adequate precision. Electronic-structure changes are captured using a semi-empirical level of theory, ZINDO, which is parametrized for reproducing the excited states (Olbrich and Kleinekathöfer, 2010). All free-energy values have convergence error, but they are commensurate with the thermal noise at room temperature, ca. 0.6 kcal/mol.
4. The coarse-grained MD Martini model does not describe the internal dynamics of proteins. Therefore, changes in the structure that could potentially be induced by lipids cannot be observed (Marrink and Tieleman 2013). An elastic network approach, called Elnedyn, was applied to the bc_1 complex to maintain the protein structure close to the initial configuration of the atomistic protein used to generate the coarse-grained model (Periole et al., 2009). Limitations of the Martini model are discussed in more details in Marrink and Tieleman (2013) and Corradi et al. (2019). Similarly, the Brownian dynamics (BD) simulations is able to access the millisecond timescale, but only at the cost of compromising with the internal degrees of freedom – the diffusing proteins are described as rigid bodies. Both coarse-grained MD and the BD simulations are refined in all-atom detail using MD

and bias-exchange umbrella sampling to determine more accurate energy changes and kinetic barriers. Thus, within convergence errors, our rate computations remain physically relevant.

5. Finally, our ATP-turnover model describes a stationary state of constant light input and ATP output. While this state is biologically relevant, it is also only a special case of constant irradiation. In the case of substantial motion of bacteria through their habitats or under a cycle of dark-to-light transitions, the current model will not be able to predict the growth correctly, as the molecular-scale phenomenon will change.

List of Abbreviations

Reaction Center (RC); Light-harvesting (LH); Cytochrome c_2 (cyt c_2); Atomic-force microscopy (AFM); Molecular dynamics (MD); Quantum mechanics/Molecular mechanics (QM/MM); Brownian dynamics (BD); Potential of mean force (PMF); Adaptive Poisson Boltzmann Solver (APBS); Oak Ridge Leadership Computing Facility (OLCF); Coarse-grained (CG); All-atom (AA); Atom Resolved Brownian Dynamics (ARBD); Bias-exchange umbrella sampling (BEUS); Steered MD (SMD); Thin layer chromatography (TLC); Fourier Transform Infra-Red (FTIR); Electron Paramagnetic Resonance (EPR); Nuclear Paramagnetic Resonance (NMR).

QUANTIFICATION AND STATISTICAL ANALYSIS

Detailed error analysis is provided in the Methods section to judge the convergence of the QM/MM, MD and BD simulations, as well as the limitations of the chromatophore model. Data is presented either using histograms/bar-diagrams (dipole orientation, excitation energy and binding time) or as mean and standard deviations in trend of physical properties (radius of curvature, free energy, diffusion and protein composition) to show the uncertainties in computational and experimental measures. Barring the 0.5 μs MD and 40 μs CG simulation of the chromatophore, all other QM/MM, MD or BD simulations were repeated between 6 to 500 times (Table 1). Uncertainties in atomic positions is represented by experimentally determined beta-factors from the PDB models, and subsequently using root mean square deviations of the MD-refined model. To avoid overfitting of the computational with experimental cell doubling times, two separate ATP yields were considered in the kinetic model. Using just one value of ATP yield clearly misses to explain the data. All the spectroscopic measurements for determining chromatophore composition, and subsequently, the cell doubling times were repeated five different times.

DATA AND CODE AVAILABILITY

The accession number for the modeling, simulation and analysis input files used in this article is Mendeley Data: https://data.mendeley.com/datasets/hh3kv79k7w/1

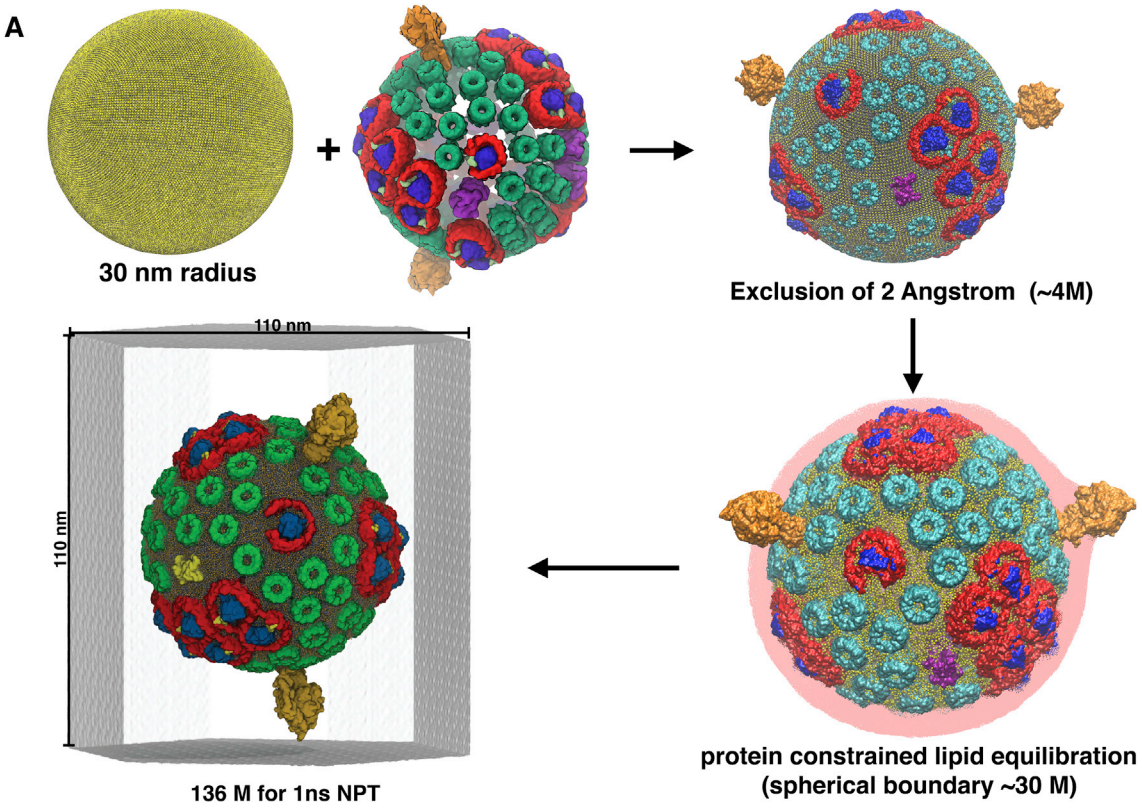

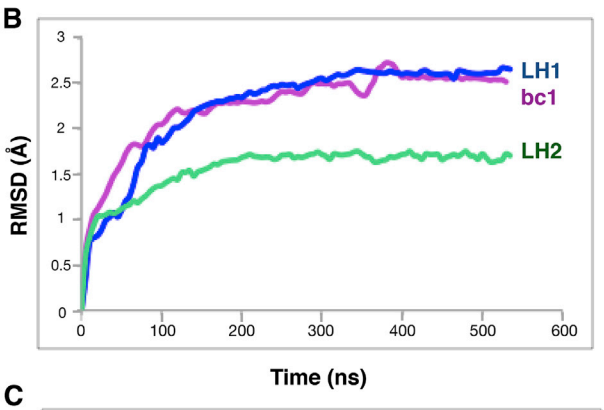

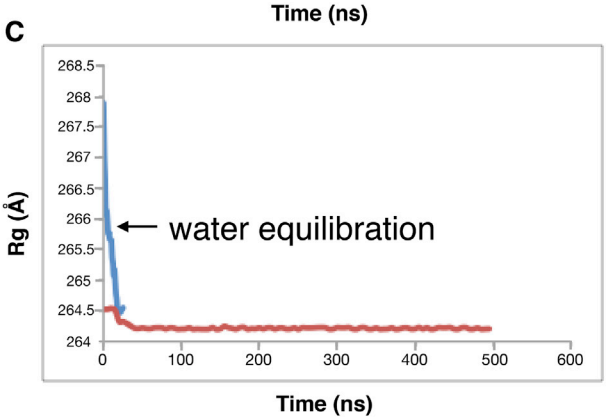

(legend on next page)

Figure S1. Workflow for the Construction of the Initial Chromatophore Model, Related to Figure 1

(A) Protein-only model of the chromatophore vesicle derived from AFM, electron microscopy and mass spectrometric data (Cartron et al., 2014) is overlaid with a POPC-only lipid vesicle of radius 30 nm to uniformly construct a lipid bilayer on protein-excluded areas of the chromatophore surface; a 2 Å exclusion radius, employed for the lipid placement around proteins, suffices to avoid unfavorable steric interactions between the proteins and the lipids. System size of this protein-embedded lipid vesicle is 30 M atoms. The vesicle is immersed in a water droplet, wherein the lipid molecules are allowed to relax under spherical boundary conditions for a period of 2 ns (0.5 ns with the lipid-head and the proteins constrained to initial position, and the remaining 1.5 ns with just the protein constrained). The partially equilibrated lipids are then heterogenized by randomly mutating the PC-head groups to PG and PE (Chandler et al., 2014) under compositional restraints of 22% POPC, 22% POPG and 56% POPE on the outer (cytoplasmic) side and 24% POPC, 10% POPG and 66% POPE on the inner (periplasmic) side, compositions consistent with lipid measurements in photosynthetic bacterial membranes. In addition, 900 charge-carrier quinone molecules were randomly introduced in the membrane, 600 of uniformly distributed and the other 300 were co-located in the vicinity of the quinone-binding bc_1 and RC-LH1 complexes. Finally, the lipid and quinone-corrected chromatophore model is placed inside a water cube of approximate dimensions 110 nm and ionized to neutrality, constituting a simulation system of size 136 M atoms. An octagonal box is presented here for visualization of the system, as rendering of the complete system is not yet feasible due to hardware limitations. (B) Root mean square deviation (RMSD) plotted as a function of simulated time showing that bioenergetic proteins have been sufficiently equilibrated over 0.5 μs. Consistent with simulations of a flat chromatophore patch (Chandler et al., 2014), the RC-LH1 dimer is found to be the most flexible and LH2 the least flexible even when the chromatophore assembles as a vesicle. (C) Change in the radius of gyration of the vesicle showing a drop of 4 Å during the final 25 ns of model refinement stage (water equilibration), wherein the protein-lipid packing tightens and lipid composition reorganizes in the vicinity of the proteins, following which the value plateaus reinstating the achievement of a stable chromatophore model.

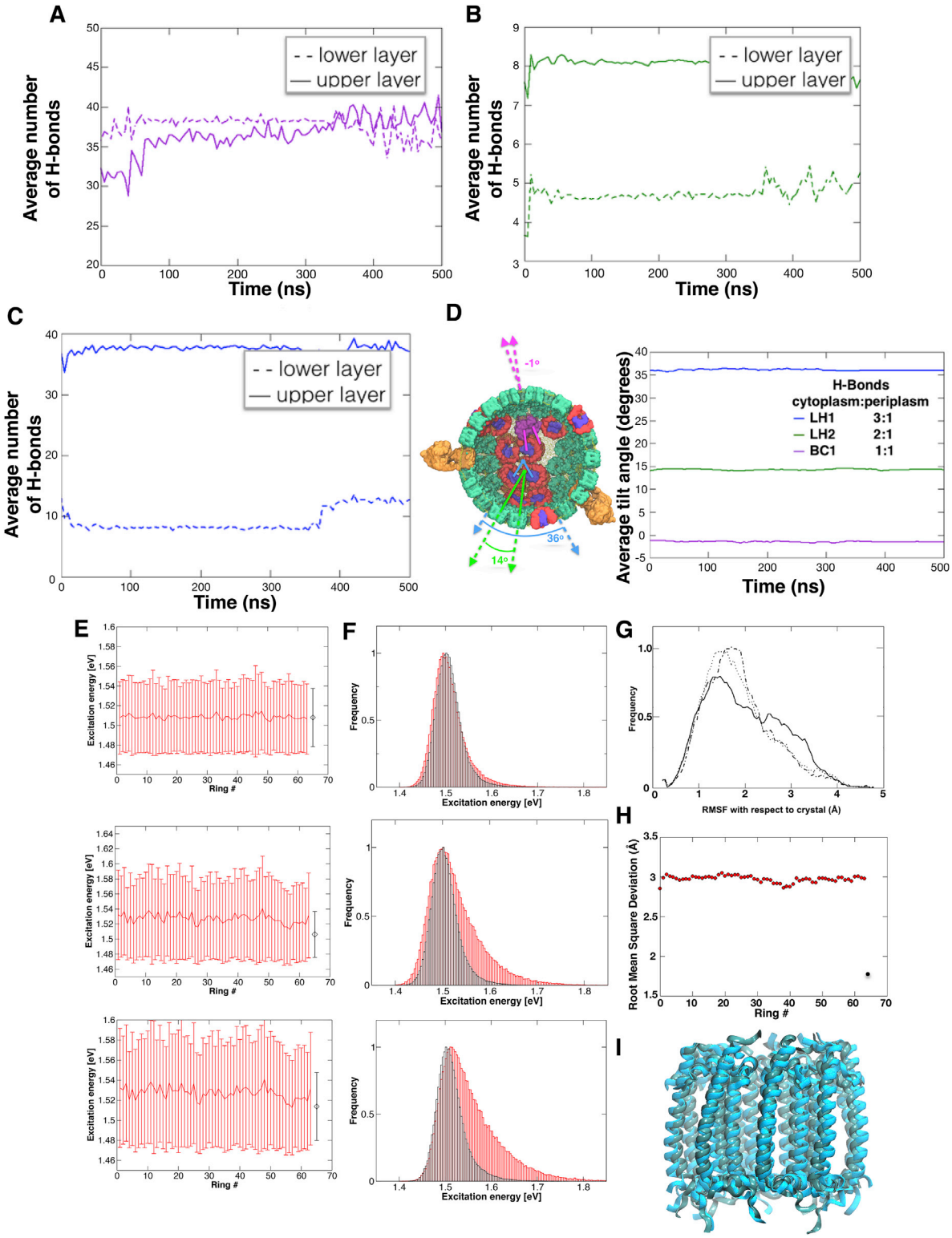

Figure S2. Hydrogen Bond Analysis of the Chromatophore Model and Ring-Wise Energy Distribution of Pigments, Related to Figure 2

Plots showing the number of hydrogen bond between proteins and lipids on the upper versus lower leaflet of bc_1 (A), RC-LH1 (B) and LH2 proteins (C). Unlike bc_1, RC-LH1 dimers form 3 times more hydrogen bonds on the cytoplasmic side, while LH2 complexes form 2 times more hydrogen bonds. (D) Local membrane curvature of the chromatophore proteins. Tilt angle induced by RC-LH1, LH2 and bc_1 proteins showcasing different extent of curvature induced by these proteins.

(legend continued on next page)

Computed from Equation 3 (Method Details), while RC-LH1, LH2 induce a closed (convex) curvature of radius 20 nm, bc_1induces a minimally open (concave) curvature of radius of −0.07 nm. (E) Excitation energy of pigments B850α (top), B850β (middle) and B800 (bottom) for all 63 LH2 complexes in the chromatophore. For a specific pigment-type in a given LH2 ring all 9 excitation energy values are considered. These energy values are collected over all frames of the QM/MM simulation to determine the mean and the standard deviation (shown as error bars) for the particular ring. The last ring with number 64 shows the data for the individual ring in a flat membrane. (F) Distributions of excitation energies in BChl B850α (top), B850β (middle) and B800 (bottom) for the simulation of a single ring in a flat membrane (black) and for all rings in the chromatophore (red). (G) Distribution of RMSF for each pigment across all the 63 LH2 rings in the chromatophore relative to their crystallographic conformation, showing B800 (solid) varies the most and B850α (dotted) the least. During the RMSF computations individual LH2 rings from the chromatophore trajectory are aligned to those from the crystal; this process is repeated for all the 63 rings. Since the pigments are not individually aligned, this RMSF metric remains sensitive to translational and rotational changes, representing thus the overall positional variance (Singharoy et al., 2013) of the pigments, beyond simple fluctuations. (H) RMSD of individual LH2 rings with respect to crystal structure 1NKZ. The red circles represent the 63 rings from chromatophore, and the black circle imply an isolated LH2 on a flat membrane. (I) Structural snapshots showing deformation of the LH2 architecture between the flat (green) versus curved membrane (cyan).

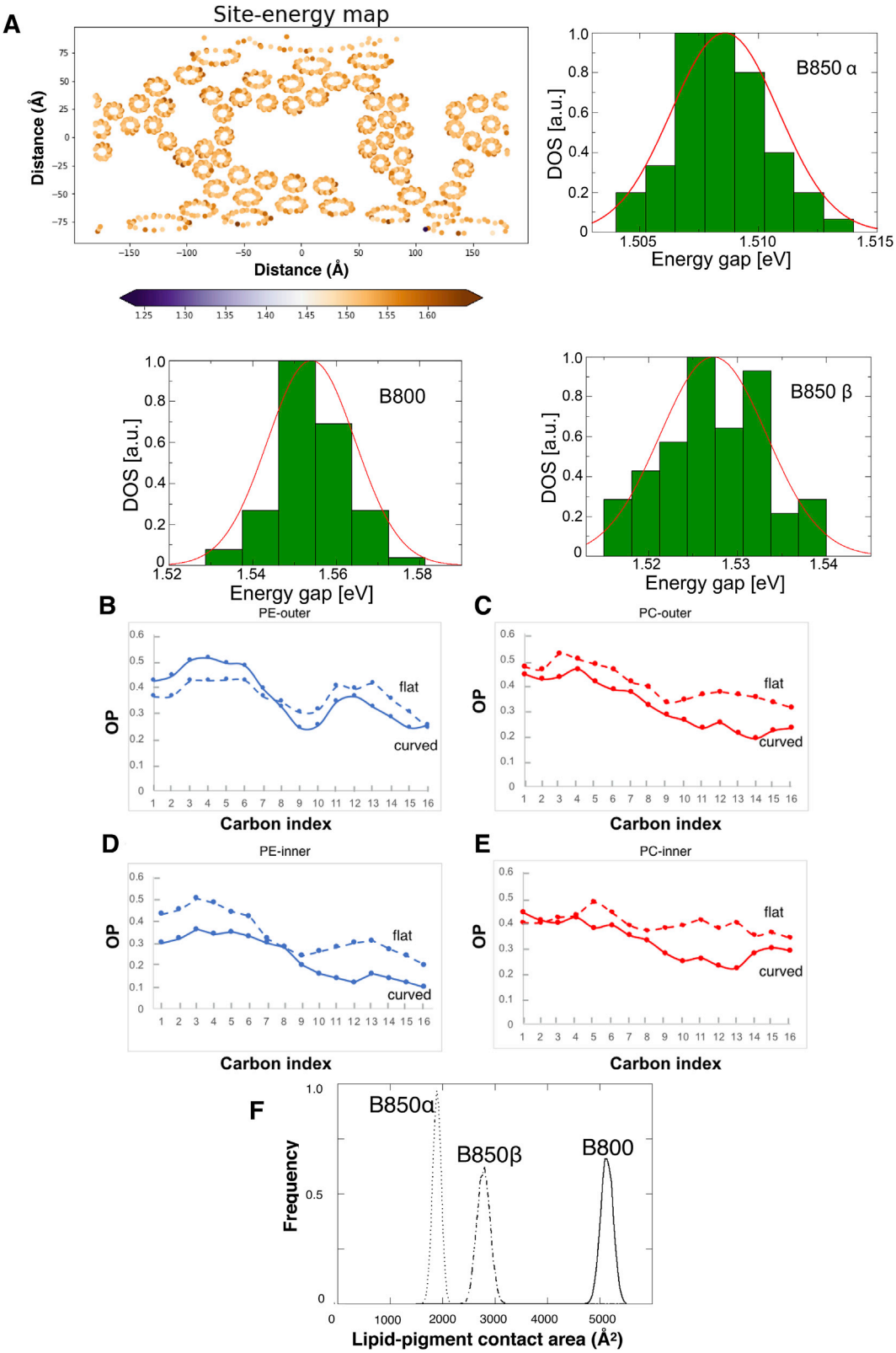

(legend on next page)

Figure S3. Influence of Environment on the Average Excitation Energies of the BChl Molecules and Lipid Order Parameters (OPs), Related to Figure 3

(A) Distributions of the average excitation energies for the different rings. The data shown in the histograms has been averaged over the nine pigments of the same BChl type within a ring and over time. (B-E) OPs plotted against the index of carbon atoms on the tail of POPC (blue) and POPE (red) lipid molecules for outer and inner leaflets of LH2 embedded flat (dashed-line) and curved chromatophore (solid-line) membrane. Lipids in the curved membrane are found to be consistently more disordered. (F) Lipid-pigment contact area per LH2-ring in the chromatophore, showing B800 is the most lipid-exposed and B850α is the least.

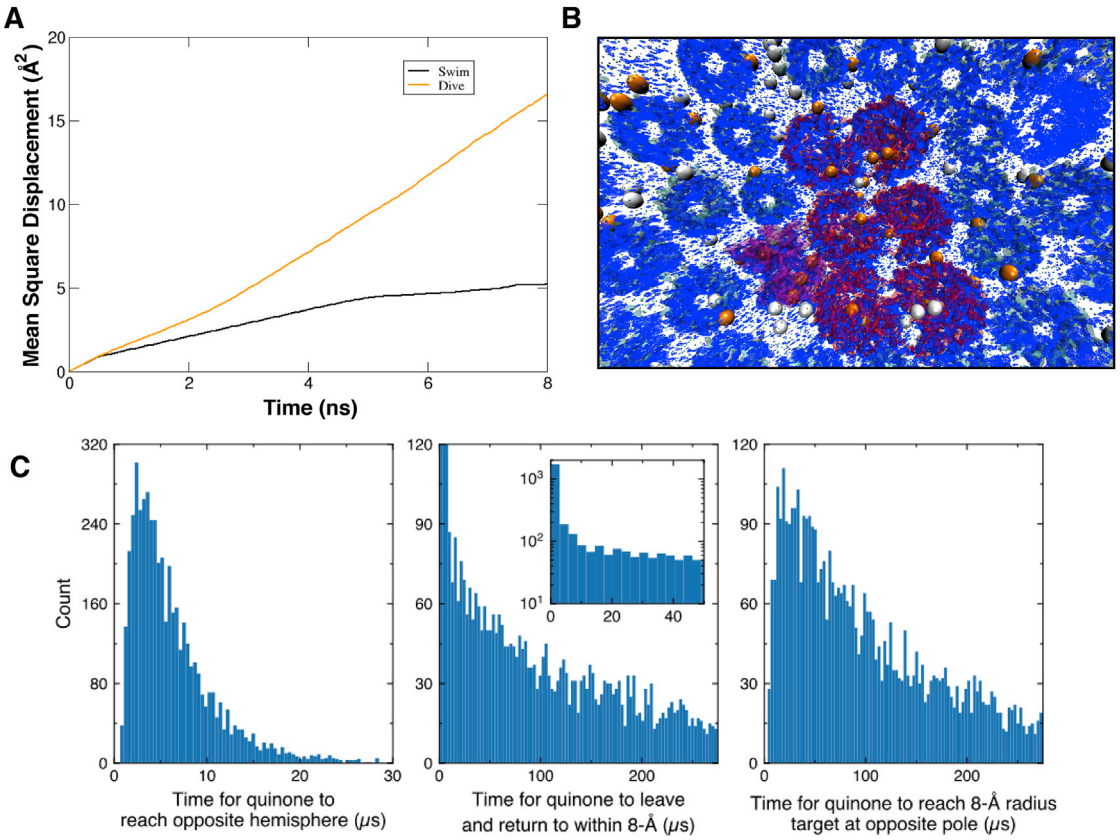

Figure S4. Swimming versus Diving Quinone, Related to Figure 4

(A) Mean square displacement (MSD) of the swimming (black) and diving (orange) quinone molecules. Clearly discernible from the plot, slope of the diving quinone is thrice as steeper than that of the swimming one. The diffusion coefficients derived from these MSD plots are 5×10^{-8} cm^2/s for swimming and 1.5×10^{-7} cm^2/s for diving. (B) Membrane-wide view of swimming (white) and diving (orange) quinone molecules illustrating that the former is more probable away from the protein-lipid interface, while the latter is significant close to the protein networks, depicting thus a state stabilized by the positive electrostatic potential (blue) in the vicinity of the proteins. (C) Timescale of quinone motion through the chromatophore are extracted. All three panels show data from BD simulations of 5000 quinone molecules independently moving through the chromatophore. The leftmost panel shows the distribution of times required for each quinone molecule to move from its initial position to the opposite hemisphere of the chromatophore (average 6.3 μs). The second panel depicts the time required for a quinone that had moved at least 16 Å from its initial location to return to within 8 Å of its location (average 68 μs). As shown in the inset, nearly half of the quinone molecules returned to their initial location within just a few microseconds. The rightmost panel depicts the time required for a quinone molecule to reach an 8-Å-radius target on the opposite side of the chromatophore (average 101 μs). Using an 8-Å-radius target as a proxy for a protein, the typical time required for a quinone to reach any particular protein in the chromatophore can be expected to be 68-101 μs.

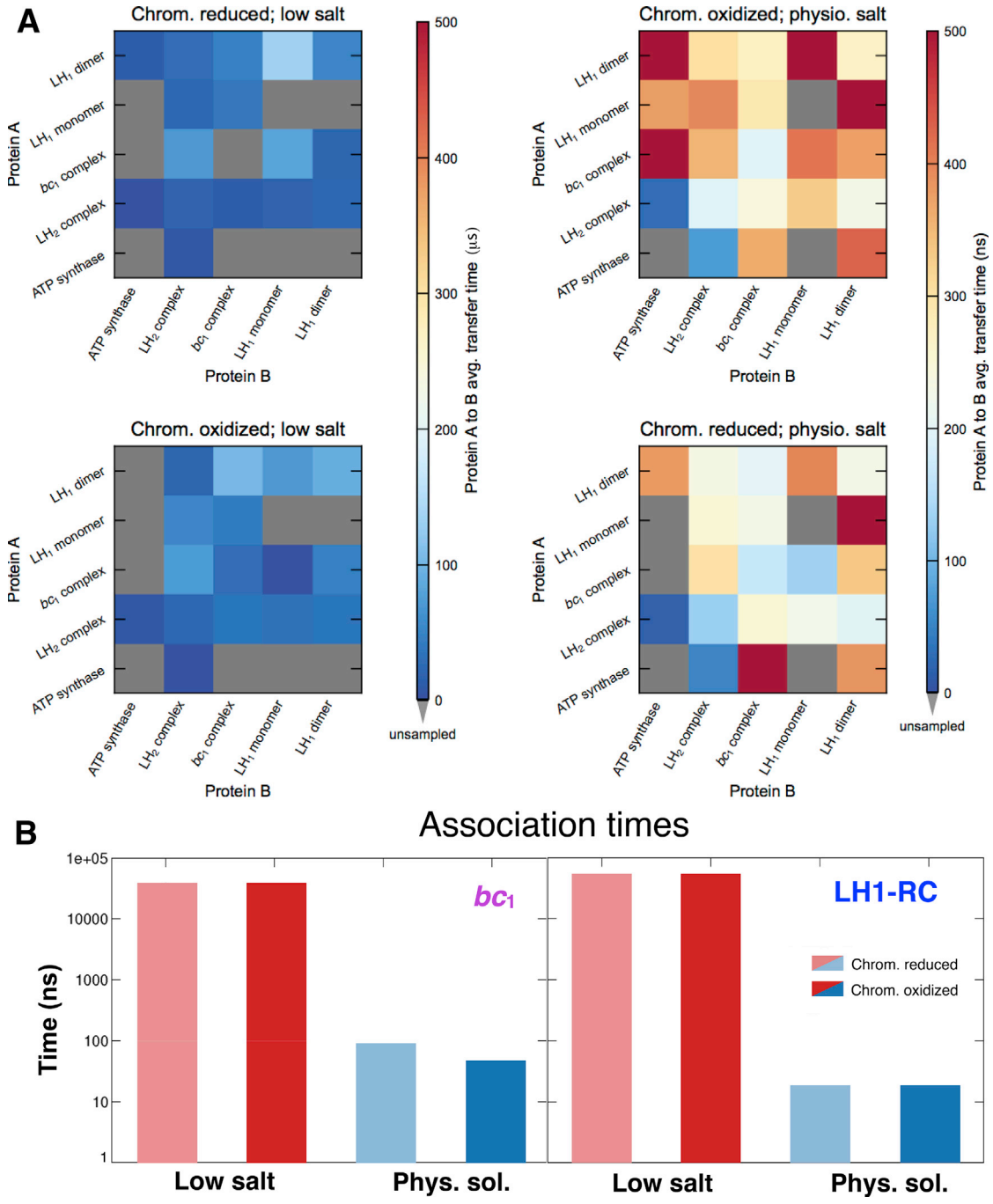

Figure S5. Kinetics of Cyt c_2 Shuttling between Chromatophore Proteins, Related to Figure 5

(A) The heatmaps depict the times required for cyt. c_2 to move between protein complexes on the chromatophore surface as observed in BD simulations. The cyt. c_2 starting site is labeled on the x axis and the landing-site is labeled on the Y-axes, and the color on the block implies time taken to move between these two sites. Four solution and electronic conditions are depicted. Motions at lower-salinity are generally slower than under physiological conditions. Furthermore, the 100-500 ns inter-complex cyt. c_2 diffusion time (off-diagonal blocks) is found to be comparable to the timescale of association dynamics in Figure S5B, but much faster than that 1 ms and 71 ms timescale of cyt. c_2 binding (Figure S7D) under physiological or low salinity concentrations. (B) Association times of cyt. c_2. BD simulations at physiological and low salt conditions reveal association times of cyt. c_2 to bc_1 (left) and RC-LH1 (right) increases drastically with drop in salinity from 150 mM to 20 mM. Association time is defined as the lifetime of a cyt. c_2-bound bc_1 or RC complex, with interface separation of 12 Å or lesser.

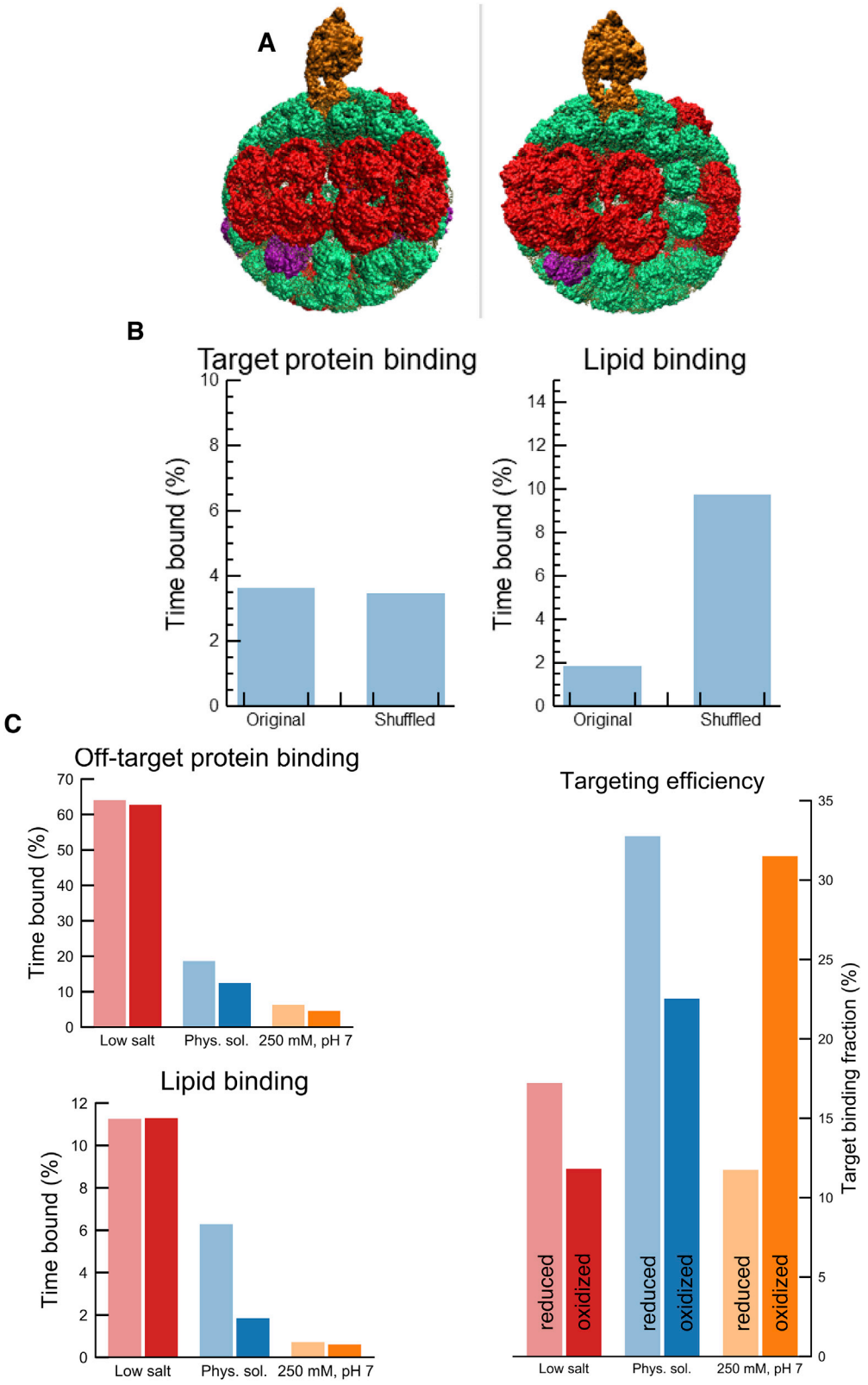

(legend on next page)

Figure S6. Protein and Lipid Binding of the New Chromatophore Model and Salinity Dependence of Cyt c_2 Turnover, Related to Figure 5

(A) The rearranged or shuffled model (left) and the original model (right). In the shuffled model the RC-LH1 dimer has been moved to make a row of four, according to Chandler et al. (2014). (B) Protein and lipid binding of the new chromatophore model. Target protein binding (left) and lipid binding (right). While the shuffled model does not show much variation in target protein binding, the lipid binding is more enhanced. (C) BD simulations of cyt. c_2 dynamics was performed at pH 4-0.02 M salinity, pH 7-0.15 M salinity and pH 7-0.25 M within the reduced and oxidized chromatophore. For each condition, 500 simulations of a single cyt. c_2 were performed, each simulation lasting 10 μs. The cyt. c_2 molecules were all initially in the center of the chromatophore. The trajectories provided the time the cyt. c_2 spent within 1 nm of off-target proteins, lipids and target proteins, as depicted in the bar charts at left. Although surface binding is overall enhanced, the targeting efficiency, or the ratio of the likelihood of being in contact with a target-protein compared to an off-target protein, is considerably reduced under low salinity conditions, as shown in the bar chart at right.

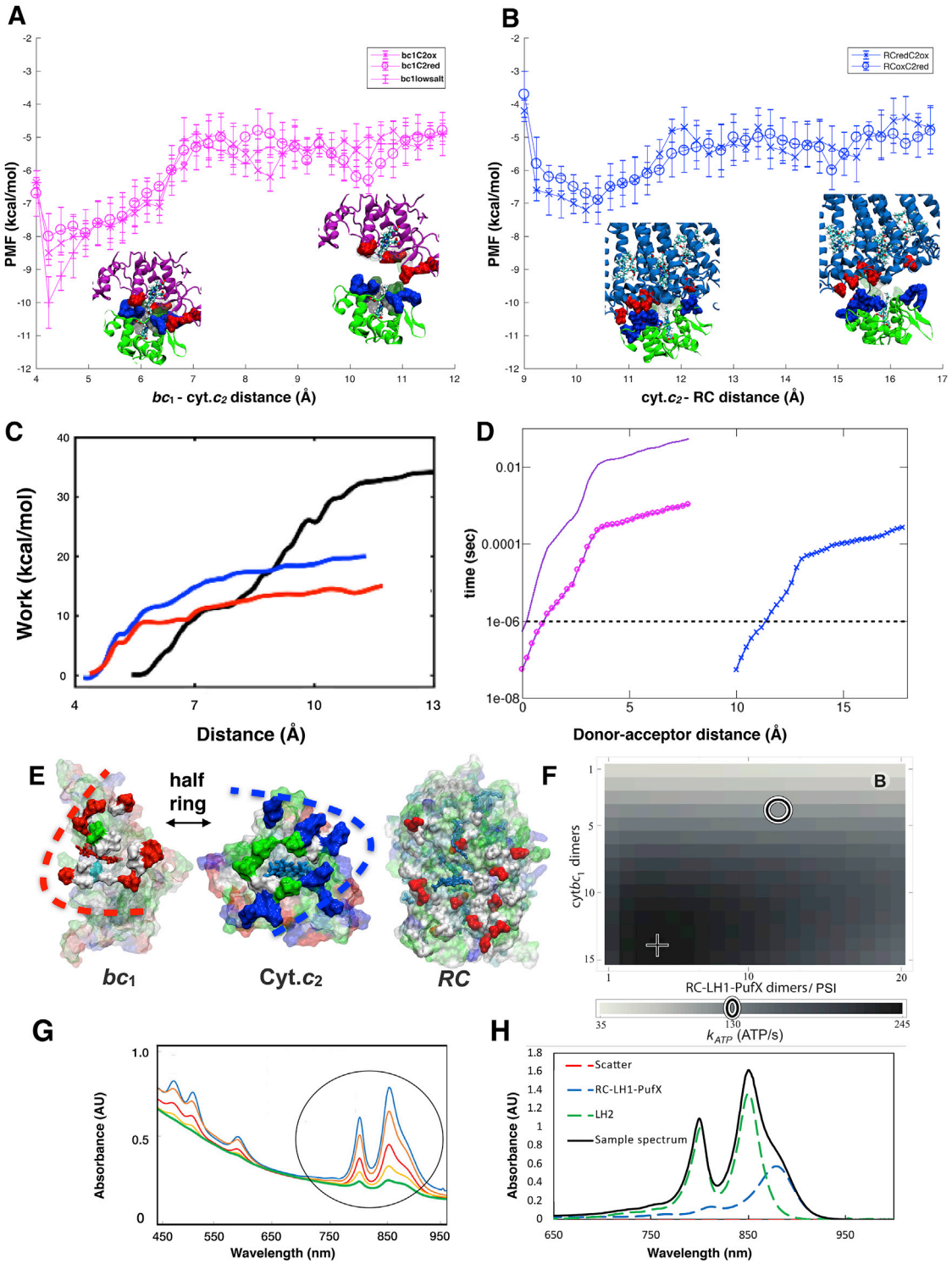

Figure S7. Free Energy of Cyt c_2 Dissociation and Effect of Vesicle Composition on Steady-State ATP Production at 3% of Full Daylight, Related to Figure 6

Potential of mean force (PMF) as a function inter-heme CBC distance derived from a cumulative 17 μs of umbrella sampling simulations describe the dissociation profile cyt. c_2 from the bc_1 complex (A) and RC proteins (B). This cyt. c_2 dissociation is monitored at four different redox states, two before and two after the electron transfer. The pre-electron transfer state features: bc_1red-$c_2$ox when the electron is in the bc_1 complex, and RCox-$c_2$red when the electron is in the cyt. c_2; the post-electron transfer state features: bc_1ox-$c_2$red when the electron is delivered to cyt. c_2, and RCred-$c_2$ox when the electron is delivered to RC. Cyt. c_2

(legend continued on next page)

binding to bc_1 complex is stronger than to RC, as also evident from the interface separation which is smaller for the bc_1-cyt. c_2 complex than RC-cyt. c_2, and specificity of the binding residues which forms a well-defined half-ring pattern in bc_1 unlike in RC (see Figure S7E). For both the bc_1 complex and RC, the cyt. c_2 binding interface weakens after electron transfer has occurred, i.e., after delivery of the electron from bc_1 complex to cyt. c_2 or from cyt. c_2 to RC. Thus, the free energy of the reduced interfaces is always more than that of the oxidized one. Reduced salinity alleviates screening effects on the dominant electrostatic interactions at the interface, and consequently makes cyt. c_2 binding to the bc_1 complex more favorable. (C) Nonequilibrium work as a function of cyt. c_2 displacement in derived from SMD simulations. The work for unbinding cyt. c_2 in bc_1ox-$c_2$red (red), bc_1red-$c_2$ox (blue) and bc_1ox-$c_2$red at 20 mM salt (black) are presented. (D) Rate of cyt. c_2 dissociation on protein surface. Mean first passage time of reduced cyt. c_2 unbinding to reduced bc_1 complex at native (magenta) and 20 mM (magenta-rings) salt strength, and reduced cyt. c_2 binding to oxidized RC, again at native salt strength (blue-cross) derived from the Szabo-Schulten equation (Szabo et al., 1980). (E) Directed interface interactions render bc_1-binding more time-consuming than RC, as cyt. c_2 faces larger entropic barriers to correctly align its half-ring residues with those of bc_1 for generating a productive complex amenable to bc_1-to-cyt. c_2 electron transfer. (F) Vesicle composition is given in terms of the number of bc_1 dimers and of RC-LH1 complexes for vesicles featuring identical surface area. The ring indicates the composition of our current chromatophore model, and the cross indicates the composition for generating highest ATP yield. Figure presentation adapted from Sener et al., 2016. (G) Whole cell spectra for *Rba. sphaeroides*. Whole cell absorbance cell spectra for measuring chromatophore content in *Rba. sphaeroides* at 1 μmol $m^{-2}s^{-1}$ (blue), 10 μmol $m^{-2}s^{-1}$ (orange), 30 μmol $m^{-2}s^{-1}$ (red), 100 μmol $m^{-2}s^{-1}$ (yellow), and 500 μmol $m^{-2}s^{-1}$ (green). (H) Spectroscopic results indicate the change in LH2:LH1 and bc_1:LH1 ratio with respect to that at the physiological 0.15 M salt concentration is minimal for salinity range between 0.10 and 0.35 M.